11-2019

Contribution of Contact Line Heat Transfer in an Evaporating Meniscus and Characteristics of Microlayer in Contact Line Region of an Oscillating Meniscus

Ishan Dabri
iud4304@rit.edu

Recommended Citation

Dabri, Ishan, "Contribution of Contact Line Heat Transfer in an Evaporating Meniscus and Characteristics of Microlayer in Contact Line Region of an Oscillating Meniscus" (2019). Thesis. Rochester Institute of Technology. Accessed from

Contribution of Contact Line Heat Transfer in an Evaporating Meniscus and Characteristics of Microlayer **in Contact Line Region of an Oscillating Meniscus**

By

ISHAN DABRI

A Thesis Submitted in Partial Fulfillment of Requirements for the Degree of Master of Science in Mechanical Engineering

Approved By:

Dr. Satish G. Kandlikar
Department of Mechanical Engineering (Thesis Advisor)

Dr. Robert Stevens
Department of Mechanical Engineering (Examiner)

Dr. Alfonso Fuentes-Aznar
Department of Mechanical Engineering (Examiner)

Dr. Jason Kolodziej
Department of Mechanical Engineering (Department Representative)

Rochester Institute of Technology

Rochester, New York 14623

November 2019

Contribution of Contact Line Heat Transfer in an Evaporating Meniscus and Characteristics of Microlayer **in Contact Line Region of an Oscillating Meniscus**

By

ISHAN DABRI

A Thesis Submitted in Partial Fulfillment of Requirements for the Degree of Master of Science in Mechanical Engineering

DEPARTMENT OF MECHANICAL ENGINEERING

Kate Gleason College of Engineering

Rochester Institute of Technology

Rochester, New York 14623

November 2019

Abstract

In nucleate pool boiling, a thin film is formed under the nucleating bubble in the region where the solid, liquid and vapor phases meet. This is called the three-phase contact line region. High rates of heat transfer have been observed in this region. Researchers have developed a pool boiling apparatus with laser interferometry and artificial nucleation sites to observe the changes in thickness, frequency, velocity and the dynamic contact angle of the microlayer. Similarly, multiple meniscus studies have been conducted to observe the characteristics of microlayer in pool boiling and various other applications such as ink jet printing, miniature heat pipes, spray cooling and drop wise condensation. In this research we look at the effect of temperature on dynamic micro contact angle and contact line velocities on a heated and polished copper surface. An apparatus was designed to oscillate a meniscus on the same copper surface. The meniscus was fed liquid to compensate for the evaporation thus making the meniscus stable. A laser source and an optical camera were incorporated to analyze the three-phase contact line region. The effect of the perimeter of the base of the meniscus and frequency of oscillating meniscus was studied. Contribution of contact line heat transfer was reported, and characteristics of microlayer formed in the contact line area of an oscillating meniscus were observed over one oscillation period.

Acknowledgement

I would like to take this opportunity to thank everyone for their support and guidance. I am extremely grateful to Dr. Satish G. Kandlikar for giving me the opportunity to be a part of Thermal Analysis, Microfluidics and Fuel Cell Lab and work under his guidance. You have been a constant source of encouragement. I feel privileged to have worked under your guidance and learned from you which only made me a better engineer.

I would also like to thank the committee members for taking out the time to review and evaluate my thesis. I would like to thank Aranya Chauhan, Aniket Rishi and all the other TAMFL members, for their support and my friends – Sudhanshu Sengaonkar, Sanket Pahade and Farhan Mody for helping me.

Contents

Abstract ... 3

Acknowledgement ... 4

Figure Index ... 7

1. Introduction ... 10
   - 1.1. Boiling ... 11
   - 1.2. Contact Line Region ... 15
   - 1.3. Interferometry ... 17
   - 1.4. Contact Angle ... 20
   - 1.5. Contact Angle Hysteresis ... 21
2. Literature Review ... 22
   - 2.1. Meniscus Evaporation ... 22
   - 2.2. Microlayer Evaporation ... 24
   - 2.3. Sessile Drop Evaporation ... 29
3. Objectives ... 34
4. Experimental Apparatus ... 35
   - 4.1. Interferometry Setup ... 35
   - 4.2. Experimental Apparatus – Oscillating Meniscus ... 37
   - 4.3. Chip Polishing ... 39
   - 4.4. Test Section ... 40
   - 4.5. Methodology ... 41
   - 4.6. Data Acquisition ... 42
   - 4.7. Method to calculate the thickness of the film with MATLAB ... 43
   - 4.8. Validation of Interferometry ... 46

4.9. Uncertainty Analysis ... 48
5. Results ... 52
5.1. Thickness Profile of Thin Film Evaporation at Various Temperatures ... 53
5.2. Contact Line Velocity and Contact Angle vs Surface Temperature ... 56
5.3. Conversion of Partial Pressure to Wall Super Heat ... 57
5.4. Evaporation of Static and Oscillating Meniscus ... 58
5.5. Volume of Static meniscus Over Time ... 59
5.6. Oscillating Meniscus Volume ... 60
5.7. Calculation for determining Heat Transfer Coefficient ... 62
5.8. Heat transfer through Surface Area and Contact Line of meniscus ... 63
5.9. Heat Flux vs. Wall Superheat and Effect of Diameter – Static Meniscus ... 65
5.10. Effect of Frequency on Oscillating Meniscus ... 66
5.11. Characteristics of Microlayer in an Oscillating Meniscus ... 67
6. Conclusion ... 70
7. Future Work ... 72
References ... 74

Figure Index

Figure 1. Pool Boiling Curve 12

Figure 2. Schematic of different region of contact line [1]........ 15

Figure 3. Concept of Interference. 18

Figure 4. Interferometry in microlayer. 18

Figure 5. Similarity between interference pattern in an air wedge and microlayer. 19

Figure 6. Contact angles for hydrophilic and hydrophobic surfaces. 20

Figure 7. (a) Advancing and (b) Receding contact angle [2]. 21

Figure 8. Microlayer in a steady meniscus........ 24

Figure 9. Utaka's [21] apparatus for microlayer beneath a nucleating bubble. 26

Figure 10. Thickness Profile – Utaka[25]. 27

Figure 11. Gao et al [20]. - Schematic and thickness profile of the microlayer. 28

Figure 12. (a) Representation of a pinned droplet. Radius is fixed, contact angle and height decrease with time. (b) Representation of triple line jump [29]. 31

Figure 13. Evaporation of an ethanol droplet with TiO2 nanoparticles [29]. 32

Figure 14. Schematic of the setup. (a) Liquid supply through syringe pump. (b) Using the laser source for interferometry. The syringe is moved out of the path........ 35

Figure 15. A close view of the chip and heater........ 36

Figure 16. Schematic of apparatus for oscillating meniscus........ 37

Figure 17. Schematic of combined apparatus - interferometry and oscillating meniscus........ 38

Figure 18. Test section - not to scale. 40

Figure 19. Positions of thermocouples for measurement of temperature of surface and meniscus. 42

Figure 20. Droplet as seen through the optical lens........ 44

Figure 21. (a) Area of the droplet seen on the screen. (b) Points marked on the contact line to interpolate the radius at t=0s. 44

Figure 22. Thickness profile corresponding to Figure 15(a) and 15(b), for surface at 40°C. 45

Figure 23. Experiment on air wedge for validation. 46

Figure 24. Fringe spacing measurements. 47

Figure 25 Bias and Precision uncertainties 48
Figure 26 Bias uncertainty in thermocouple 49
Figure 27. Advancing and Receding contact angle on polished copper surface. 52
Figure 28. Four stages of drop evaporation. 53
Figure 29. Evaporation of thin film. 54
Figure 30. Thickness profile of an evaporating thin film at 23.8 °C. 54
Figure 31. Average contact angle (AVG CA) and average contact line velocity in an evaporating thin film. 56
Figure 32. Static meniscus from side view and Volume of Revolution 58
Figure 33. Volume of static meniscus over time. 59
Figure 34. Minimum and maximum positions in an oscillating meniscus. 60
Figure 35. Meniscus volume at minimum position of an oscillating meniscus at 0.6 Hz frequency. 61
Figure 36 Meniscus volume at minimum position of an oscillating meniscus at 0.6 Hz frequency 61
Figure 37 Percent Heat transfer through Surface Area of meniscus and Contac Line region 64
Figure 38. Effect of diameter on heat flux vs wall superheat. 65
Figure 39. Circumferential heat transfer vs wall superheat. 65
Figure 40 Heat transfer per base length for various frequencies and effect of contact angle on the heat transfer per unit base length. 66
Figure 41. Evolution of microlayer in an oscillating meniscus. 67
Figure 42. Thickness profile of microlayer formed in an oscillating meniscus at 60 °C – 0.6 Hz. 68
Figure 43. Variation of micro contact angle in the microlayer of an oscillating meniscus in one frequency. 68
Figure 44. Maximum and minimum position of contact line at t = 0s and t = 0.6s - 0.6 Hz, 30 °C. 69

Table Index

Table 1. Heat transfer coefficient for different modes of heat transfer 11

Table 2 Comparison of thickness profiles from the literature... 55

Table 3 Constants of Nusselt Number equation for circular cylinder cross flow – Zukauskas relation 62

1. Introduction

In today's rapidly advancing world, technology is moving towards achieving more efficient systems. Effective heat transfer is a major concern in electronics, nuclear and power generation, and other industries where the devices must be maintained in a specific range of operational temperatures. In the electronics industry, for example, devices operate at a higher power density due to the advances in miniaturization of electronic components. In the nuclear industry, the nuclear core must be maintained far from the melting temperature of the core material to prevent a possible nuclear catastrophe. In the power generation industry, the increasing demand of electric energy pushes engineers to increase the efficiency of the heat transfer processes. This requires a high amount of energy transport at small temperature differences, especially at small scales. This pushes the conventional heat transfer methods to extract high amounts of energy. Air cooling and single-phase liquid cooling are used to dissipate low amounts of heat off the system to meet their operational limits. Newer technologies like two-phase heat transfer are known to have heat transfer coefficients as large as 100, 000 W/m^2-K as compared to 10,000 W/m^2-K in single phase cooling. Table 1 shows the comparison of heat coefficient values by various methods and of various fluids. The ability to have such high heat transfer coefficients demands the advancement of research in this field.

Boiling involves a phase change which can dissipate large amounts of heat due to the formation of vapor bubbles which carry a large amount of heat with them. However, boiling is a very complex and chaotic phenomenon which is very difficult to study.

Table 1. Heat transfer coefficient for different modes of heat transfer

Process	**Fluid**	**Heat Transfer Coefficient (W/m^2-K)**
Natural Convection	Air	2 – 25
	Water	50 – 1000
Forced Convection	Air	25 – 250
	Water	100 – 20,000
Pool Boiling	**Water**	**2,500 – 100,000**

1.1. Boiling

Boiling has proven to be an effective way of cooling. It is a phenomenon in which a fluid undergoes the phase change from a liquid to a gaseous state. The latent heat of a liquid is much greater than the sensible heat. Hence a two-phase cooling is accompanied by large amounts of heat transfer. Boiling can further be classified as pool boiling and flow boiling. In pool boiling, a stagnant pool of liquid is heated by a heater surface. The main source of heat transfer in pool boiling is due to the bubble growth which remove heat from the surface as they grow and depart. Flow boiling consists of incoming liquid on the heater surface which then changes its phase, taking heat off from the surface. Even though flow boiling is related to very high amounts of heat transfer, there exists many challenges such as pressure drop and non-uniform flow rates that cause instability in the system. However, both pool boiling and flow boiling processes are limited by a phenomenon known as Critical Heat Flux (CHF), the situation in which the entire heater surface gets covered with a thin layer of vapor. When the surface hits this point, the temperature of the heater surface jumps up by a few hundred degrees in a very short time. The result of this can be potentially dangerous and can melt down the heater surface and system. Figure 1 shows a typical pool boiling curve.

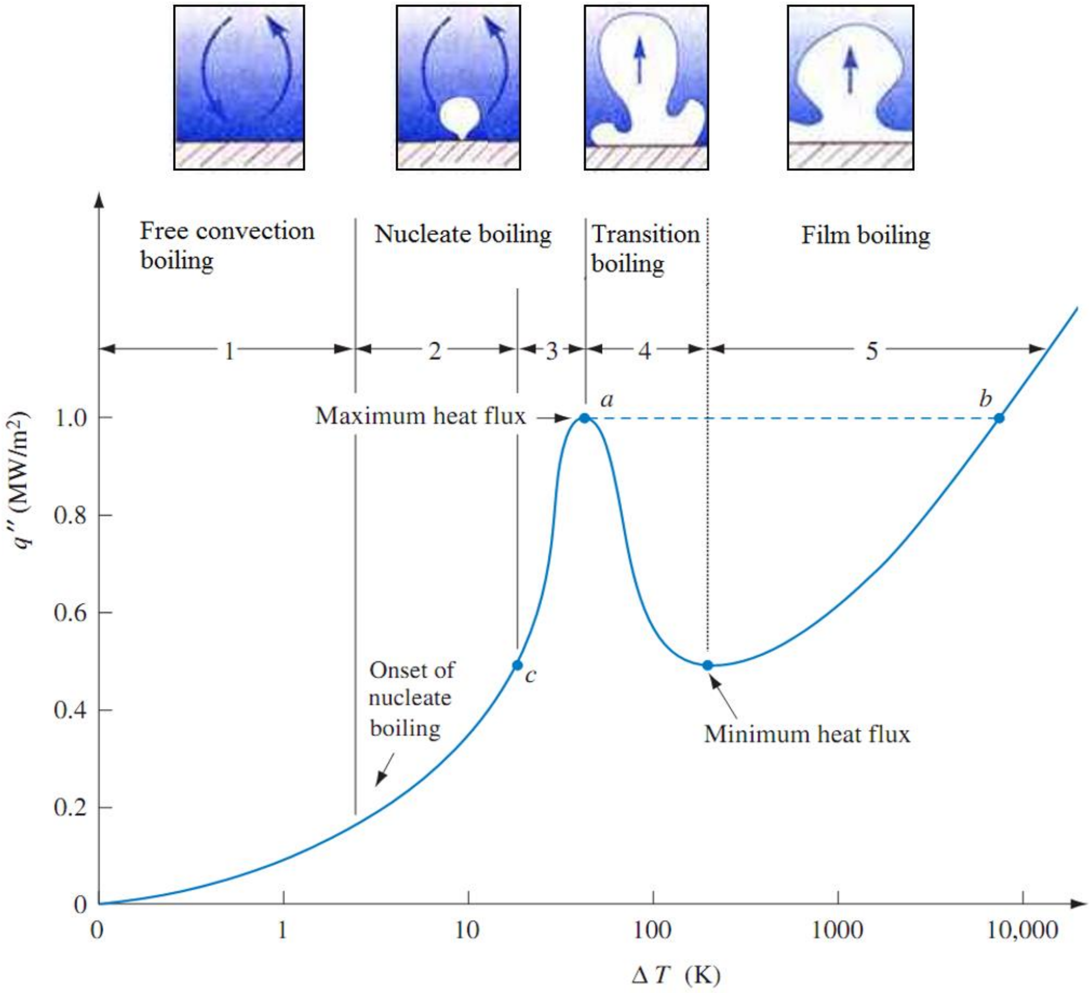

Figure 1. Pool Boiling Curve

The boiling curve is divided in four regimes –

1. Natural Convection
2. Nucleate Boiling
3. Transition Boiling
4. Film Boiling

1. Natural Convection

The first region is where the heat transfer takes place through natural convection. The bulk liquid in the vicinity of the heater surface is comparatively hotter than the rest of the pool above it. This gives rise to the natural flow of liquid due to the difference in the temperature. The wall superheat (difference between saturated liquid and surface temperature) is not significant for the nucleation of bubbles on the heater surface. As the temperature is increased and the liquid attains its saturation temperature, the nucleation of bubbles starts. This point is called the Onset of Nucleate Boiling (ONB).

2. Nucleate Boiling

As the temperature rises further, more bubbles are observed at various locations on the heater surface. The nucleation sites also get activated with the temperature rise. This results in higher heat flux and higher heat transfer coefficients. This region is called partial nucleate boiling. The region between the points ‘c’ and ‘a’ (as indicated in Figure 1) is called developed nucleate boiling. With further increase in the surface temperature the frequency of bubble nucleation increases. This increase in bubble formation results in coalescence of bubbles forming vapor columns at certain locations. As the heat flux is increased further, the vapor bubbles start coalescing upward and sideward. With further increase in the temperature Critical Heat Flux (CHF) is reached (‘a’). As point ‘a’ is reached, a vapor blanket is formed on the surface as a result of coalescence of bubbles. The temperature of the surface shoots up. In real-time situation, the transition boiling period is extremely low and the curve directly jumps from point ‘a’ to ‘b’ (as indicated in Figure 1).

3. Transition Boiling

Once the vapor film collapses, the curve rapidly transfers from region 4 to 2 through the region 3. This is known as transition boiling. It is very difficult to achieve a steady state as the wall superheat increases with increase in the heat flux.

4. Film Boiling

The region 5 shown in Figure 1 is called film boiling as the heat is conducted to the bulk liquid through a vapor film and the temperature of the surface is very high as the heat transfer through vapor is very poor. When the heat flux is steadily decreased, the wall superheat also decreases. With enough decrease in the surface temperature, the vapor blanket collapses, and the curve enters into transition boiling region.

1.2. Contact Line Region

The three-phase contact line is where the three phases intersect – solid, liquid, and gaseous in a nucleating bubble. A microlayer is formed under when a bubble nucleates on a heated surface. This is explained in detail in the literature review section. Recent advancements in contact line have concluded that high heat transfer rates take place in this microlayer region (Figure 2). The contact line can be divided in the four regions – the adsorbed film region, transition region, intrinsic meniscus region, and macro convection region.

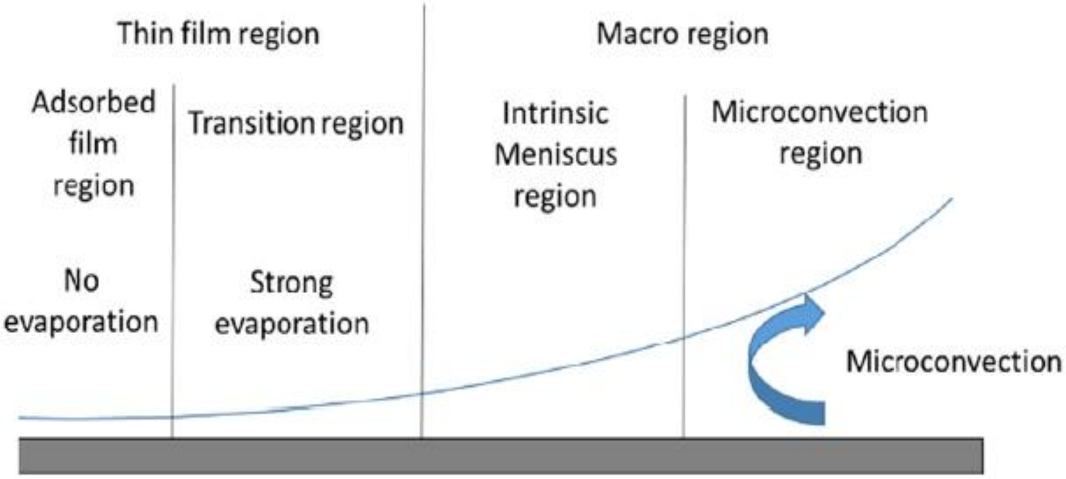

Figure 2. Schematic of different region of contact line [1].

The adsorbed film region and the transition region can also be called the thin film region, while the macro region comprises of intrinsic meniscus region and macro convection region. In the adsorbed region, there is no evaporation due to high disjoining pressure which is due to Van der Waals forces between the molecules of the liquid and solid and thus, it doesn't contribute in the growth of the bubble. In the transition region, the thickness of the film is comparatively more than that in the adsorbed region and hence, due to increase in the distances of the liquid-solid molecule, the disjoining pressure and the Van der Waals forces are low and strong evaporation rates are observed. A sharp curvature in the intrinsic meniscus region gives rise to capillary forces at the liquid-vapor interface and gives rise to high heat fluxes in this region. These high evaporation rates are because of low resistance to evaporation due to increased thickness of the film. Similarly, due to even lower thickness and reduced disjoining pressure, even higher rates of evaporation are observed. The thickness of the film increases and the resistance to evaporation also increases as we go towards the macro-convection region. Therefore, a low evaporation rate is observed.

1.3. Interferometry

Researchers have tried out various methods using special equipment to find the thickness of the microlayer. Because interferometry is easy to use compared to other methods like using a thermal analyzer, depth sensors, infrared etc., it has been selected for this research. The thickness of the meniscus is the thickness of the contact line region beneath the bubble. The measurement of the thickness using interferometry consists of a laser source, collimating lens, and high-power microscope. Interferometry relies on the interference and diffraction patterns due to the net change of the phase of the rays that are refracted from the secondary medium. For example, from Figure 3 consider the incident ray at point A which is partly reflected and partly refracted into the liquid. The ray (AB) hits the bottom of the surface and is reflected in the liquid. When the ray hits the surface, it again goes under reflection and refraction due to change of refractive indexes of the mediums (liquid and surface). The refracted ray (BC) is in phase with the reflected ray (AD) when the distance travelled by the ray in liquid (A to C) is equal to integral multiple of wavelength and a bright band is seen. When the phase difference is an integral multiple of half wavelength, the dark band is seen. As the temperature of water increases, the refractive index of water reduces and thickness *(t)* increases.

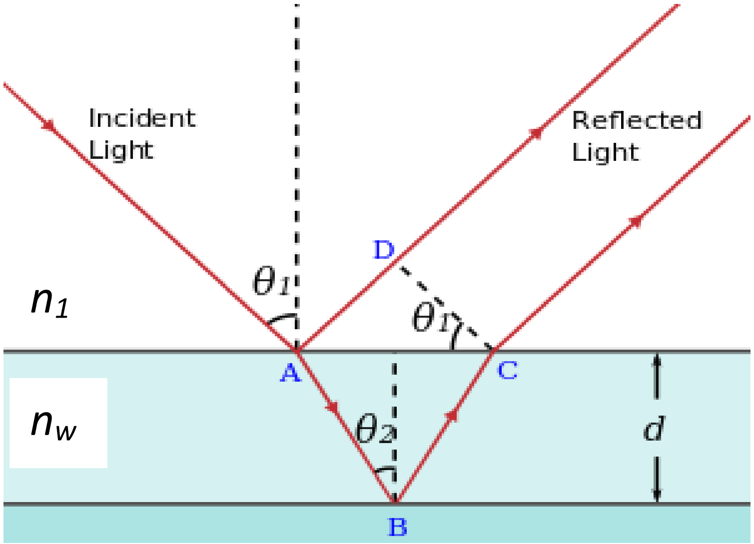

Figure 3. Concept of Interference.

$$2tn_w = m\lambda - \ for\ bright\ bands \tag{1}$$

$$2tn_w = \left(m + \tfrac{1}{2}\right)\lambda \ - for\ dark\ bands \tag{2}$$

Where, t = thickness at location m, n_1 = refractive index of air, n_w = refractive index of water, $n_w > n_1$ and λ = wavelength of light.

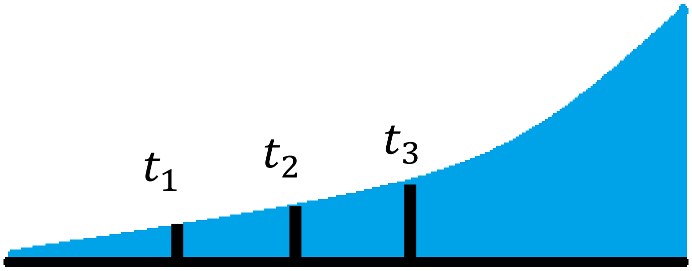

Figure 4. Interferometry in microlayer.

Assuming the contact line is the 0th dark band and the bright band is the first bright band, substituting *m* = 1 and *m* = 0 in equations 1 and 2 respectively leads to the following:

$$2t_1n_w = \left(\tfrac{1}{2}\right)\lambda \tag{3}$$

$$2t_2 n_w = \lambda \tag{4}$$

$$t_2 - t_1 = \frac{\lambda}{2n_w} \tag{5}$$

The increase in distance between successive dark and bright band is given by the difference t_2-t_1. If we consider the microlayer to be a like an air wedge created by two glass pieces raised at a height h at one end, then $2t = m\lambda$ can be used to calculate the thickness at the order of band M as shown in the Figure 5. Here, M is the order of black fringe.

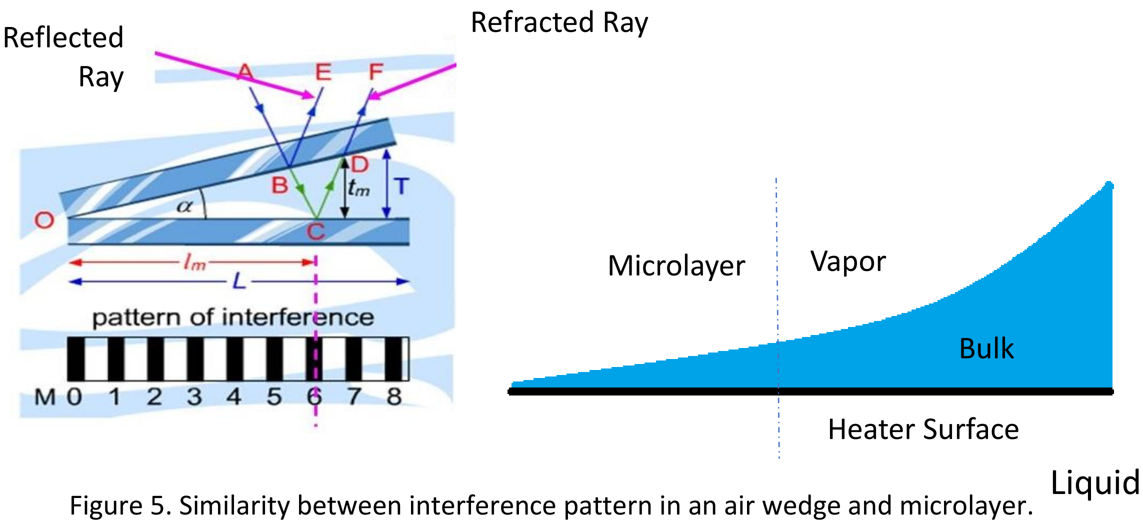

Figure 5. Similarity between interference pattern in an air wedge and microlayer.

This theory is used to calculate the thickness of the film. Here, *t* is the thickness of the liquid film, *m* is the fringe order and λ is the wavelength of light in air, and n_w is the index of refraction of the liquid. Since the thickness of the fringes is constant, due to the constant increase in thickness (constant slope), the fringe spacing, Δx, is given by the following equation.

$$\Delta x = \frac{\lambda}{2tan\theta} \tag{6}$$

1.4. Contact Angle

Contact angle is the angle measured through the liquid at the liquid-solid interface. It quantifies the wettability of the surface by liquid via Young's equation. Depending on the nature of the surface, it can be a hydrophobic or a hydrophilic surface (as shown in Figure 6). When a liquid completely wets the surface, it is called a hydrophilic surface. The contact angles in this case are low. Alternatively, when the liquid does not wet the surface, it is a hydrophobic surface. The contact angles are high on hydrophobic surfaces. Typically, surfaces with a contact angle less than 90° are the hydrophilic surfaces and the surfaces having contact angle between 90° and 180° are the hydrophobic surfaces. The factors such as surface morphology, surface roughness are further used to vary the nature of the surfaces [1].

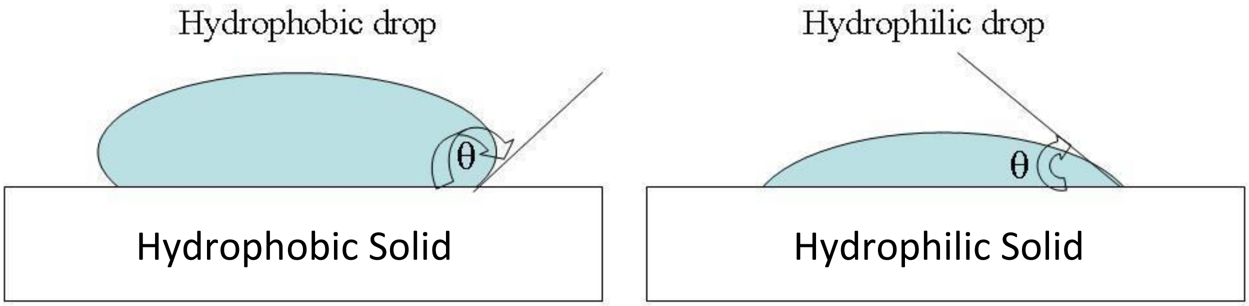

Figure 6. Contact angles for hydrophilic and hydrophobic surfaces.

1.5. Contact Angle Hysteresis

When a water drop encounters a solid surface, it forms a droplet that is a section of the sphere at a measurable contact angle with the surface. An everyday example of this can be seen in raindrops on the leaves or hood of a car. It is important to remember that when measuring the contact angle of a pair it is always measured from inside the liquid (Figure 7). When these droplets of water evaporate in an unsaturated environment or carefully withdrawn from the surface using a syringe, the contact line starts to recede. The volume and surface area of the droplet decreases with a constant receding contact angle Q_R (as shown in Figure 7a). This is a characteristic of surface topography and chemistry. Similarly, if the surface is cooler with a temperature below the dew point of the liquid or water then the liquid starts to condense on the surface. The droplet volume and surface area grow over time with a constant contact angle Q_A (as shown in Figure 7b). This is called the advancing contact angle, which is also a characteristic of surface topography and chemistry. A semi-stable droplet forms a contact angle with the surface with a value which is in between the advancing contact angle Q_A and receding contact angle Q_R. Hence, it is important to report both – advancing and receding contact angle when defining the contact angle characteristics if a liquid-solid pair.

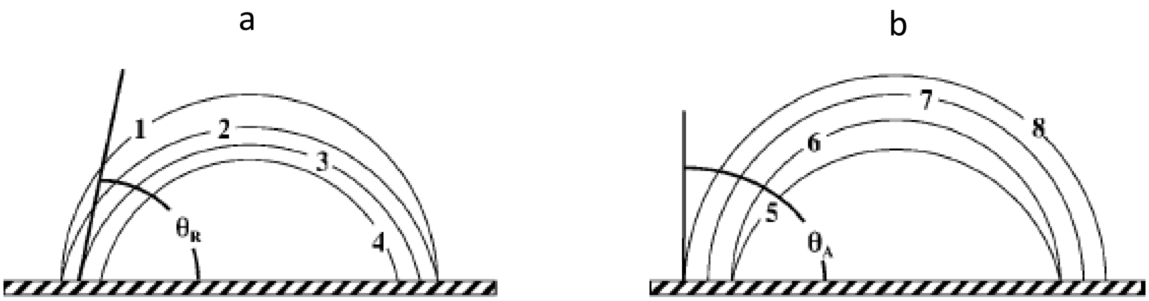

Figure 7. (a) Advancing and (b) Receding contact angle [2].

2. Literature Review

Many of the industrial processes and cooling systems which are under development or already available commercially depend on two phase flows. Two phase systems are better performing as stated in the introduction. Two phase applications like pool boiling, flow boiling, thin film boiling, and heat pipes all have vapor bubble nucleation which is in contact with the solid, liquid, and the vapor interface called as the triple contact line. If we consider a process of evaporation of a sessile droplet, it can also be a thin film covering a solid surface. The thickness of this film can be as low as approximately 10 nm [3]. This is called the adsorbed region. It has been stated that the heat fluxes in the contact line region make a significant contribution to the overall heat transfer in the system [4]. Microlayer evaporation was first proposed by Snyder and Edwards [5] as a significant contributing factor during the process of boiling which was later quantified by Cooper and Lloyd [6] by measuring the temperatures on the heater surface. This was emphasized by Demiray and Kim [7] and Raghupathi and Kandlikar [8].

2.1. Meniscus Evaporation

Stationary menisci has been the focus of for many of the previous studies in which menisci were formed inside a quartz cuvette, at the open end of a capillary tube, between two parallel plates, at the intersection of two plates and on the surface of the plate inserted in liquid at an angle.

Wayner[9] in 1978 stated that viscous flow of liquid in the contact line region affects the profile of an evaporating meniscus significantly. Theoretical analysis was conducted based on the assumption that fluid flow was caused due to London-van der Waals dispersion forces and concluded that change was due to viscous forces only and surface roughness did not have any effect. The meniscus was divided into three regions for the analysis – 1. Range of thin film near the contact line was 0 to 500 Å. 2. Intrinsic meniscus region ranged from 0.05 to 10 microns and 3. outer intrinsic meniscus where the thickness was greater than 10 microns.

Holm and Goplen[10] observed very high heat transfer rates near the contact line. This was presented by using dropwise condensation to show that surface heat transfer coefficients are ten times greater than heat transfer coefficients obtained from condensation process. In another study, Holm and Goplen used partially filled capillary grooves with liquid to form triple line region and showed that heat transfer is increased due to liquid flow in grooves as a result of capillary action. Characteristics such as - 1. Heat transfer from grooved plate, 2. Temperature drop in walls separating grooved plates and 3. Difference in temperatures of wall and surrounding vapor.

A mathematical model was formulated using the Young-Laplace equation, Van Der Wahls forces, Marangoni convection and non-equilibrium contact line conditions of a meniscus in a capillary tube by Swanson and Herdt[11]. In 1994, Hallinan et al[12] studied the effects of micropores of a heat pipe wick and characterized it by interfacial shape, temperature distribution and dispersion number on an evaporating thin film meniscus. Khrustalev and Faghri[13] developed a mathematical model for a meniscus in a capillary tube. It consisted of steady state, two-dimensional energy and momentum equation for liquid and vapor. Assumptions like constant wall temperature were made as the surface conductivity is very high as compared to the liquid. Kim and Wayner[14] used null ellipsometry and image processing and analyzing techniques to analyze evaporating thin film. Kelvin -Clapeyron model was used to estimate mass flux and interferometry images were used to plot pressure fields. Octane evaporative meniscus was formed in a closed circular cell. Some of these studies are explained in the next section.

2.2. Microlayer Evaporation

Many researchers have studied the important topic of microlayer evaporation formed under the bubble during the nucleate pool boiling process. Various methods were adopted to investigate the shape, size, and thickness but the results to date have been limited and thus further investigations are necessary for an even better understanding. Microlayer thickness has been measured using various methods like optical interferometry, temperature measurement of the heater surface using precise thermocouples, infrared imaging techniques etc. A microlayer under a nucleating bubble is shown in the Figure 8. A setup was designed to create a similar scenario but in an unsaturated environment to study the microlayer evaporation.

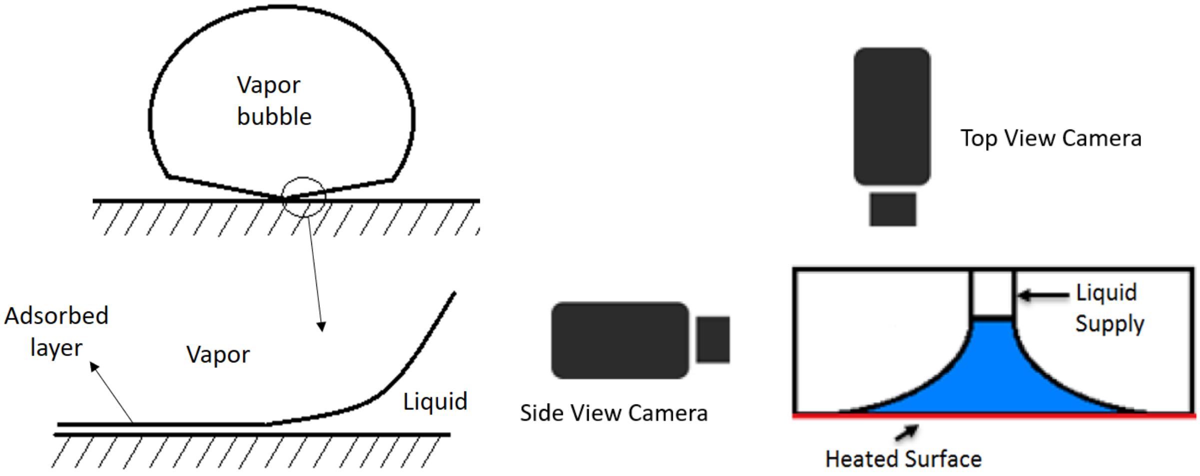

Figure 8. Microlayer in a steady meniscus.

Judd and Hwang [15] briefly summarizes the developments in this topic, starting with Sharp [16] confirming the presence of a microlayer and measured the thickness using a mercury arc lamp as a monochromatic source of light. Further interferometric studies such as Voutsinos and Judd [17] used dichloromethane and McGregor and Jawurek [18] studied the experimental errors in the interferometric techniques using methanol as a working fluid. They were able to conclude that the measurement error was less than 0.5%. Koffman and Plesset [19] studied ethanol in a subcooled boiling environment. Gao et al. [20] used a similar concept to measure the microlayer thickness with laser extinction method. Building on Cooper's [21] work in which a model is derived to calculate the heat transfer through the microlayer and bubble growth, Cooper and Lloyd [6], Van Owerkerk [22] derived an equation for heat transfer from an evaporating liquid film over a solid surface. A fundamental analysis and equation predicting the microlayer thickness was presented on a receding liquid interface by Cooper and Lloyd [6]. Adding to these studies, Graham and Hendricks [23] incorporated the transient conduction model in the microlayer heat transfer model recognizing the dynamic nature of microlayer in bubble growth and evaporation.

Kim and Wayner [14] experimentally and theoretically evaluated the heat transfer details in the contact line region using null ellipsometry and interferometry using octane as working fluid. Holm and Goplen [10], in 1979 stated that high heat transfer rates were observed near the three phase contact line. They used drop-wise condensation to show that heat transfer coefficient obtained were a magnitude greater than film condensation. Dhavaleswarapu et al. [24] in 2007 found that 95% of heat is transferred in the 30% of interface close to contact line.

Laser interferometry has been the most widely adopted technique for measuring the thickness of the microlayer under bubbles in nucleate boiling. However, this technique can only provide information about the thickness and must be coupled with high speed visualization and a strict control of the heated surface to obtain bubble structure and microlayer heated wall temperature. All the works reporting microlayer thickness have used a transparent surface heater, which makes suitable visualization from the bottom. However, in boiling applications, bubbles nucleate from metallic surfaces, for example copper or aluminum and using an opticalgrade coated surface may not reveal bubble growth characteristics relevant to further understand boiling processes.

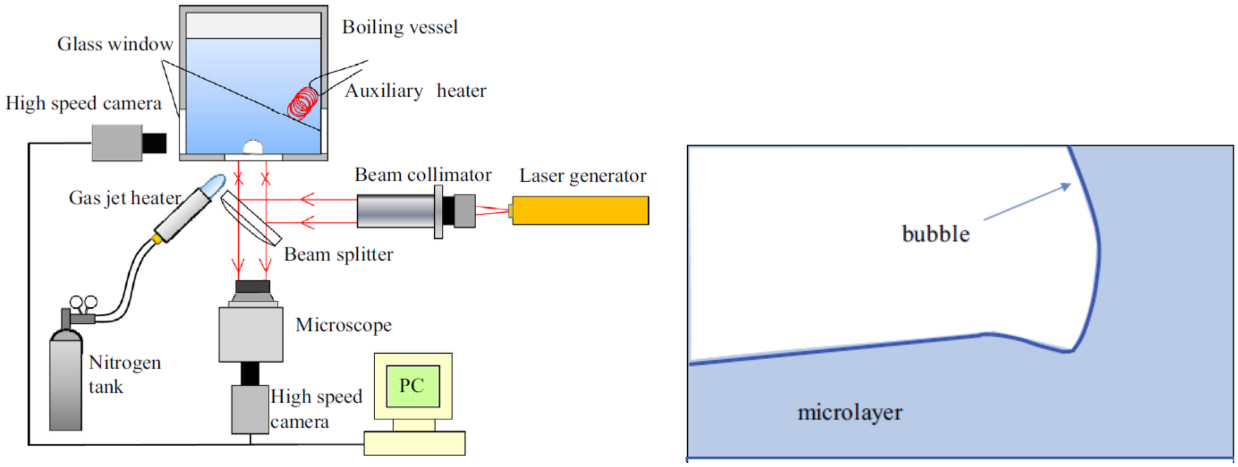

Figure 9. Utaka's [21] apparatus for microlayer beneath a nucleating bubble.

Utaka et al. [25] studied the microlayer beneath a growing bubble. A pool boiling setup was used with a quartz glass with a 2 mm diameter hole for injecting air. The plate was heated by nitrogen gas jet heater. The heat flux value was calculated using the method in[26]. A He-Ne laser with 632.8 nm was used as a light source. Figure 9 shows the apparatus used in this experiment. Utaka's group was able to conclude that the microlayer has a wedge shape but also a bended shape in a relatively larger radius and the heat flux had a very little effect on the initial microlayer thickness. In previous studies, Utaka et al. [25] were able to conclude that microlayer thickness increased linearly with increase in distance from the inception site, the initial microlayer for water was 0-9 µm thick and was twice as thick than the microlayer for ethanol. They also provided a relationship between the distance from the inception site and microlayer thickness as –

$$\delta_0 = 4.46 \times 10^{-3} r_L \text{ for water} \tag{7}$$

$$\delta_0 = 10.2 \times 10^{-3} r_L \text{ for ethanol} \tag{8}$$

where, δ_0 is initial microlayer thickness in microns and r_L is distance between bubble site and measurement location in millimeters.

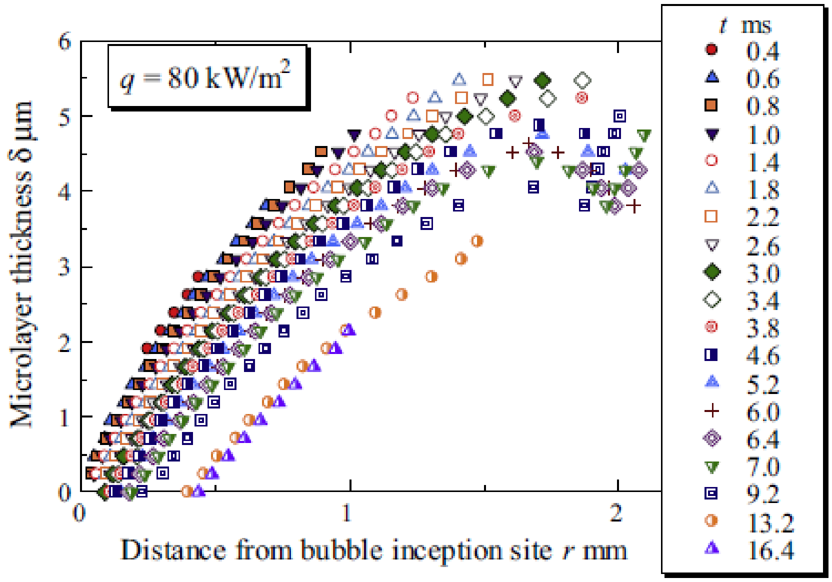

Figure 10. Thickness Profile – Utaka[25].

Similarly, Gao et al. [20] used a pool boiling setup with Pyrex glass with ITO coating as the heating surface bonded with copper sheets for joule-heating and ethanol as the working fluid. A laser source of wavelength 632.8 nm was used as the monochromatic source to record the fringe patterns beneath the nucleating bubble. They setup a relationship of dimensionless dry spot radius with a growth rate of the nucleating bubble with dimensionless time as shown in equation 1. A correlation of micro-contact angle was established with ethanol vapor bubble growth time from the equation 9.

$$\frac{r_d}{r^0{}_d} = A\left(\frac{t}{t_d}\right)^m\left(\frac{\rho_v}{\rho_l}\right)^n \tag{9}$$

where r_d is the radius of dry spot, t is the bubble growth time, ρ_v is the density of vapor, and ρ_l is the density of saturated liquid.

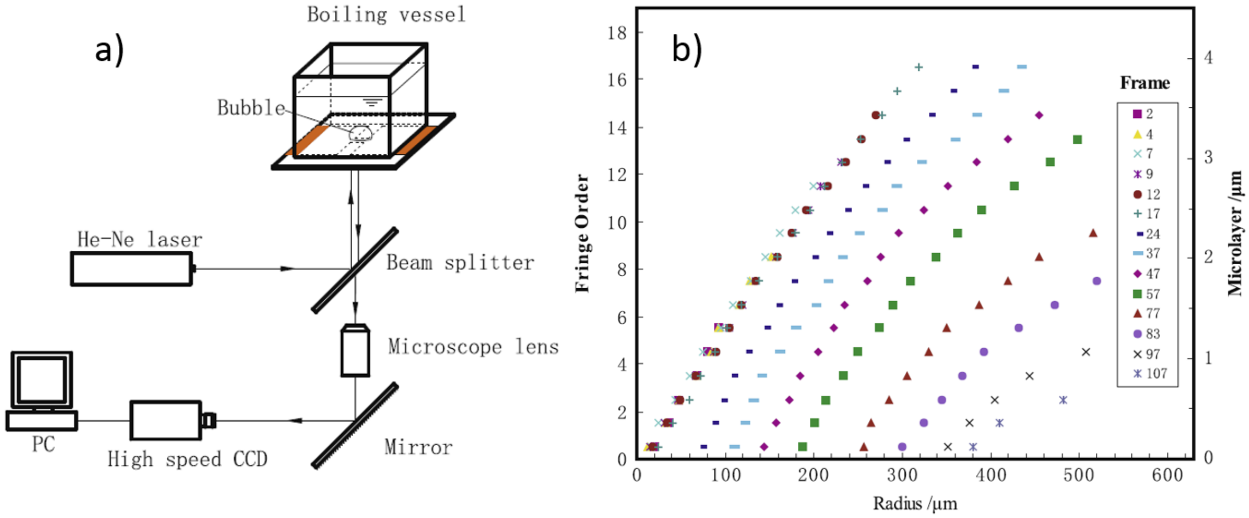

Figure 11. Goa et al [20]. - Schematic and thickness profile of the microlayer.

The schematic of the apparatus is as shown in the Figure 11. The thickness profile of the microlayer evolution over time at heat flux of 32.4 kW/m^2.

2.3. Sessile Drop Evaporation

Drop evaporation occurs in a medium with different temperatures and saturation conditions giving rise to convective circulation in the water droplet. Hence, there is no uniform temperature gradient in the droplet. Heat transfer in an evaporating droplet can occur in the form of conduction, convection or radiation. When the droplet evaporates in air, it follows a process of diffusion at air-drop interface and the rate of diffusion is limited depending on the concentration of the vapor molecules in free air. The equation for diffusion is given by –

$$-\frac{dm}{dt} = 4\pi R^2 D \frac{dc}{dR} \tag{10}$$

where, m is the mass in kg, t is the time in s, R is the radial distance from the center of the droplet (m), D is the diffusion coefficient (m^2/s) and c is the concentration of the vapor (kg/m^3). If we assume the boundary conditions c = c_S when R = R_S and c = C_∞ when R = R_∞(R_∞ is the distance of a point at distance very far from the center), integrating equation 10 gives the rate of evaporation as –

$$-\frac{dm}{dt} = 4\pi R_S D(C_S - C_\infty) \tag{11}$$

where R_S is the radius of the spherical droplet from the center to the surface and C_S is the concentration of vapor at the sphere surface (at R_S distance).

It is found that the interaction of liquid with the solid is found to vary with different surface geometries, material and hydrophobicity of the material. On an ideal (flat, horizontal, rigid, solid) surface, the equilibrium contact angle is given by Young's equation [27] as a function of surface tensions between solid-liquid, liquid-gas and solid-gas interfaces. When a droplet is placed on a surface, depending on the nature of the surface, there can be partial or complete wetting. During complete wetting, the droplet sits flat on the surface and the contact angles tend to 0°, while the partial wetting has measurable contact angles. This gives us the measure of the hydrophobicity of the surface.

For real surfaces, the equilibrium contact values vary between the advancing and the receding contact angle depending on the heterogeneities of the surface [28]. The equilibrium contact angle is obtained at thermodynamic equilibrium i.e. when no mass transfer takes place. Birdi [29] pointed out that the evaporation behavior of the droplet with contact angle greater than 90° is different than if the contact angle is less than 90°. It was found by Bourges-Monnier and Shanahan [30] that, for droplets with contact angle less than 90° the contact line is pinned and mass transfer due to evaporation is linear with time. While Cazabat [31] showed, for a non-wetting case, the mass transfer due to evaporation is non-linear. Thus, this demonstrates the effect of hydrophobicity on evolution of droplet profile. Shanahan [32] compared the droplet evaporation time to the hydrophobicity of the surface, depending on whether it is a constant radius evaporation or constant contact radius evaporation. In constant radius evaporation, the evaporation leading to a constant volume evaporation curve with time, while in a constant contact angle, the radius decreases, and it follows a power law. It is a competition between the pinning and the depinning forces. The pinning forces are due to the chemical and surface heterogeneities. The depinning forces are due to the deviation from equilibrium caused by evaporation (loss of mass). The deviation from equilibrium governs the pinning and the depinning of the triple contact line [33].

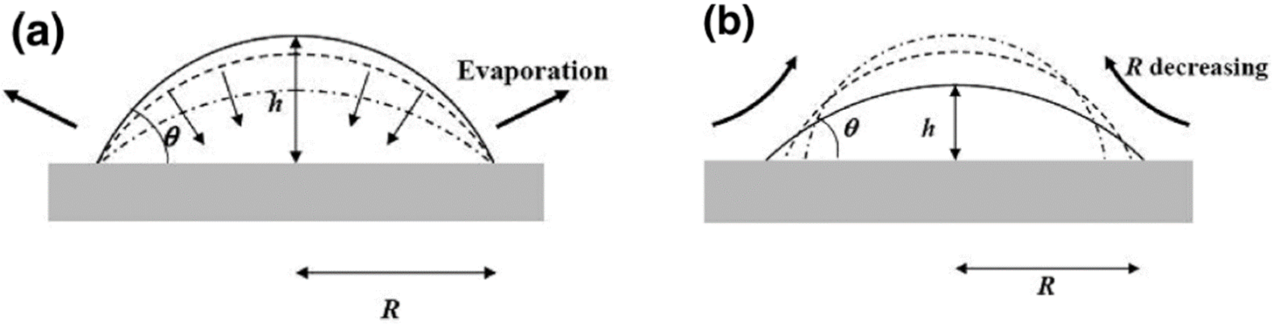

Figure 12. (a) Representation of a pinned droplet. Radius is fixed, contact angle and height decrease with time. (b) Representation of triple line jump [29].

In order to study these pinning and depinning effects, Deegan et al. [34] studied the evaporation process with colloidal particles and nanoparticles in the fluid. We know that these colloidal and nanoparticles are drawn to the periphery during the evaporation to leave a stain we call the 'coffee ring effect'. These particles are known to promote the pinning of the contact line. To better understand the effect of these particles with one another, Moffat et al. [35] found that addition of TiO_2 nanoparticles to ethanol promoted stick-shift behavior, not due to irregularities on the surface but due to nanoparticles accumulating at the contact line.

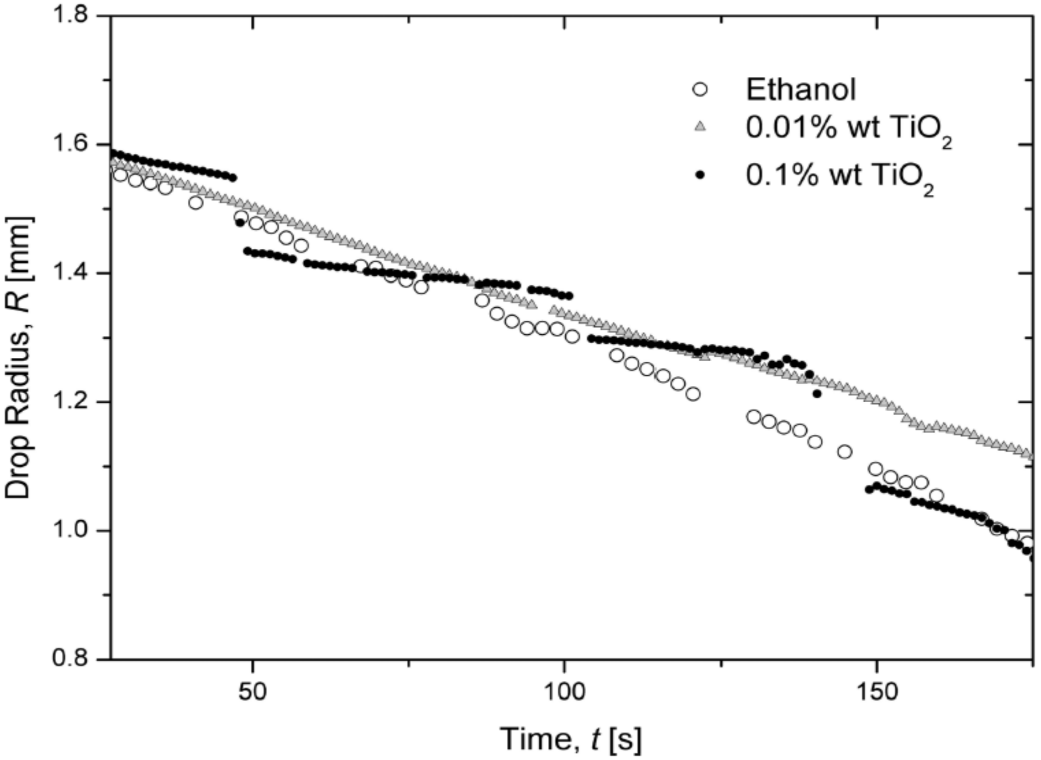

Figure 13. Evaporation of an ethanol droplet with TiO2 nanoparticles [29].

Some researchers like Li et al. [36] focused their research on the flow of nanoparticles in a droplet during evaporation. Flow inside a 0.1μL droplet was observed to be circulatory. This flow was found to be induced by pinning and depinning of the contact line. Silica particles were used, and it was found by the authors that the flow can be controlled by changing the concentration of nanoparticles or reducing surface tension by adding surfactants. Anderson et al. [37] proposed that on an ideal surface, the contact line recedes while the contact angle remains constant. On the other hand, Sefiane and Tadrist [38] found that, initially the contact angle reduces while the contact line is pinned until a limiting value is reached. After the limiting value is reached, the contact line recedes. Researchers have related the depinning force to the initial contact angle, angle before jump, and surface tension of liquid.

From this review, it is clear that microlayer evaporation and interaction of triple contact line with the surface is a complex phenomenon. With reduction in contact angle while the contact line is pinned, the height of the droplet is reduced which reduces the resistance to evaporation.

More such examples include ink-jet printing [39,40], spraying of pesticides[41], micro/nano fabrication[42,43], thin film coatings [44], biochemical assays[45], spray cooling [46], deposition of DNA/RNA micro-arrays[47–51], and manufacture of novel optical and electronic materials [52] in the last decades.

3. Objectives

As seen from the literature, various ways have been used to understand the phenomenon of microlayer evaporation. Most research that has been carried out to understand microlayer evaporation has a pool boiling setup with a transparent heater surface as ITO glass that enables the use of laser source from the bottom of the surface. Surfaces transparent to infrared have been widely used to capture thermal images of the surface to calculate the temperature difference between the microlayer and bulk liquid. Thermocouple arrays have been designed and attached to the surface to calculate the heat flux in the microlayer region. The aim of this study is to estimate the contribution to the heat transfer from the contact line region of a steady and oscillating meniscus. Along with this test, an evaporating sessile droplet on an opaque, smooth and reflective surface (Copper) was tested using interferometry and results were compared to the data reported in the literature. From high speed images on the evaporating droplets contact line velocity, dynamic contact angle and thickness profile of the evaporating thin film of water in an open-air system can be calculated.

In a pool boiling system when nucleation starts a microlayer is formed beneath the vapor bubble. The bubble oscillates at various frequencies and contact angle. The interferometry setup was combined with oscillating meniscus setup to analyze these parameters to gain insight on microlayer characteristics.

4. Experimental Apparatus

4.1. Interferometry Setup

The experimental setup is shown in the Figure 14. The He-Ne laser is used as a coherent source and has a power of 10 mW and a wavelength of λ = 632.8 nm. As the cross-section of the beam may not be a perfect circle, it is passed through an iris of a perfectly circular cross-section. The rays then pass through a collimating lens which focuses the rays on a focusing lens to increase the diameter of the laser beam. As the diameter of the ray exiting from the collimating lens is 0.5 mm, it needs to be expanded and amplified. The KEYENCE microscope captures the interference pattern. All the optical instruments need to be perfectly aligned for accurate measurements. Figure 15 shows the apparatus – Optical camera (interferometry), collimating lens test chip, syringe dispenser.

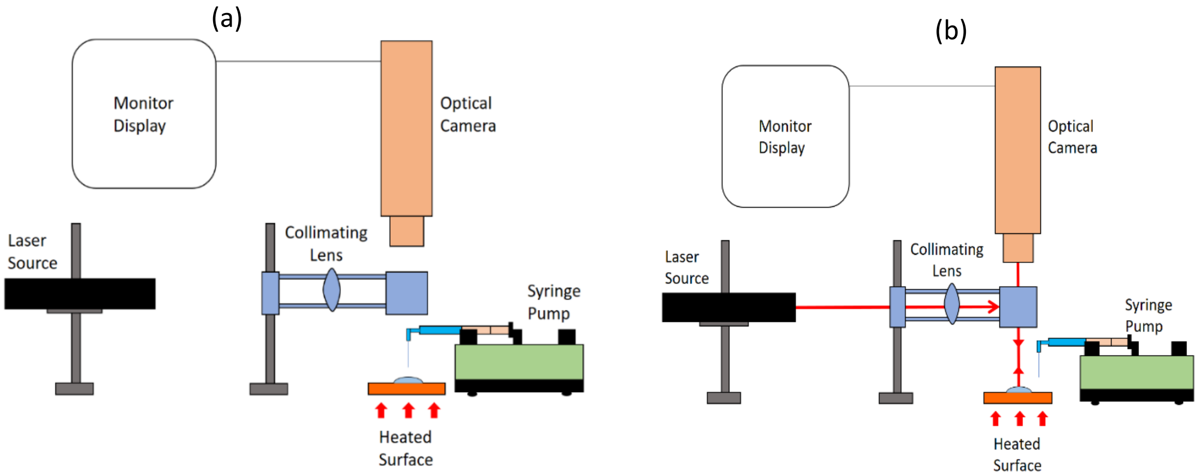

Figure 14. Schematic of the setup. (a) Liquid supply through syringe pump. (b) Using the laser source for interferometry. The syringe is moved out of the path.

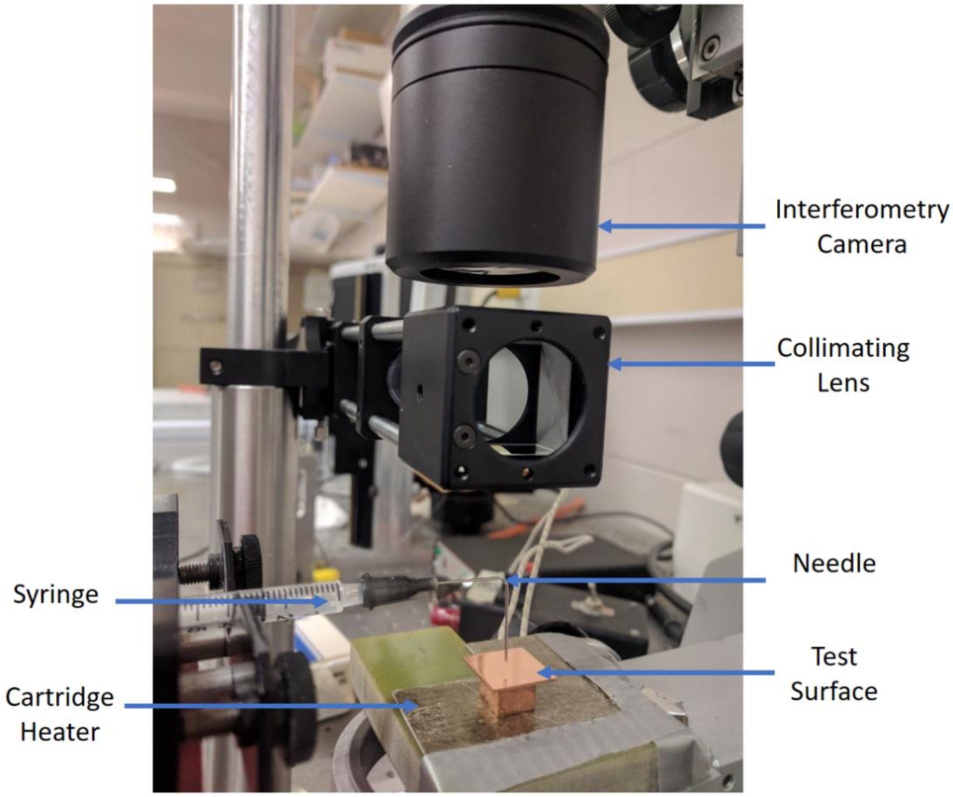

Figure 15. A close view of the chip and heater.

4.2. Experimental Apparatus – Oscillating Meniscus

The schematic of the setup is as shown in Figure 16. A stepper motor was connected to L293D microcontroller. The circuit was set up on a bread board and interfaced with an Arduino board. A potentiometer was connected to vary the speed of the stepper motor. Two syringes are connected with a three-way tube to allow flow of the distilled water which is the working fluid. One of the syringes is setup on a syringe pump which controls the movement of the piston in the syringe cylinder. This pump is interfaced with LabVIEW on a computer to achieve precise and accurate flow rates. The piston of the second syringe is connected to a reciprocating mechanism connected to the shaft of the stepper motor. As the stepper motor turns, the piston of the syringe moves up and down to vary the flow rate of the meniscus thus formed on the surface.

The interferometry and the oscillating meniscus setup were combined to analyze the microlayer that forms in a moving meniscus.

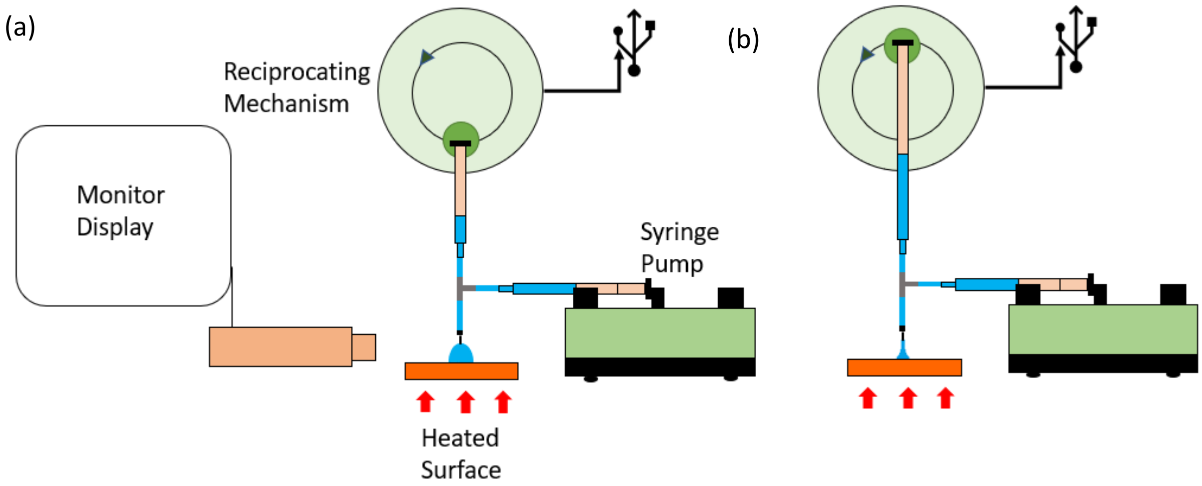

Figure 16. Schematic of apparatus for oscillating meniscus.

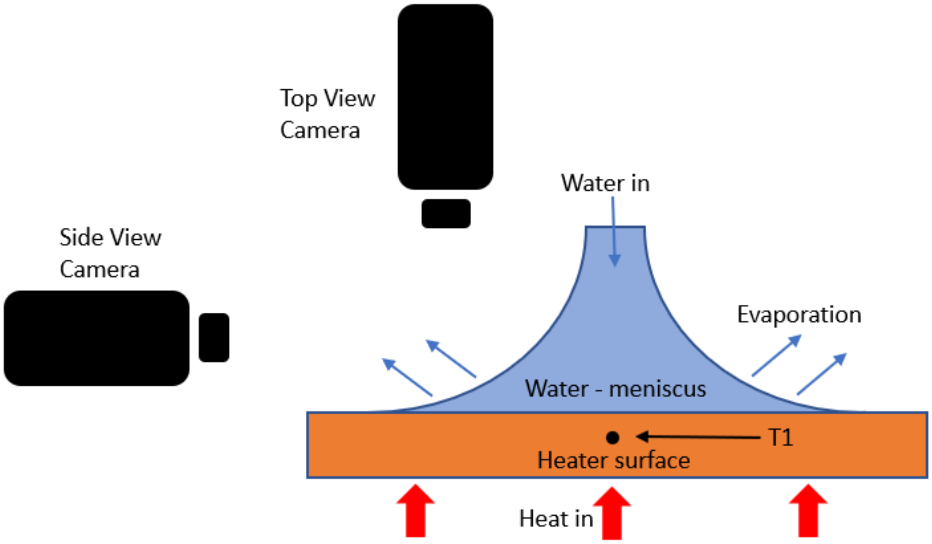

Figure 17. Schematic of combined apparatus - interferometry and oscillating meniscus

4.3. Chip Polishing

In order to obtain a good display of fringes the chip needed to be reflective and smooth. In order to make the test chip smooth and reflective, it was first ground and then polished. The test chip was polished using a Tegra Pol polishing machine on which different disks of reducing roughness and three of each grinding and polishing disc were used progressively.

Grinding operation started with using the Struers MD Piano 220 disc. The number denotes the grit size of each disk. Struers MD Piano 500 was the second disc used for the grinding operation. Struers MD Piano 1200 was the third disc used for the final grinding operation. Water was used as a lubricant during the grinding process. These discs have a resin bonded diamond surface.

For the polishing operation, a polishing cloth and water-based diamond suspension was used as the abrasive. Struers MD Plan was used for the first operation. This is a polishing cloth made of coated woven polyester and water-based diamond suspension containing diamond particles which are 9 microns in diameter. Similarly, MD Dac was used for the second operation along with Struers Dac 3 abrasive which contains diamond particles of size up to 3 microns in diameter. MD Dac is a satin woven acetate cloth. For the last polishing operation MD Floc polishing cloth was used with NapB1 which contains suspended diamond molecules whose size is up to 1 micron in diameter.

The surface was found to have surface roughness below 0.5 microns with a smooth and reflective finish.

4.4. Test Section

The test section is a flat copper chip which has been polished to under 0.5 microns roughness. Figure 18 shows the test sections used in these experiments. A cylindrical test chip was manufactured after the preliminary tests to fit the size of the polishing machine slots. This assisted in lowering the polishing time. All the preliminary tests were performed on the square chip.

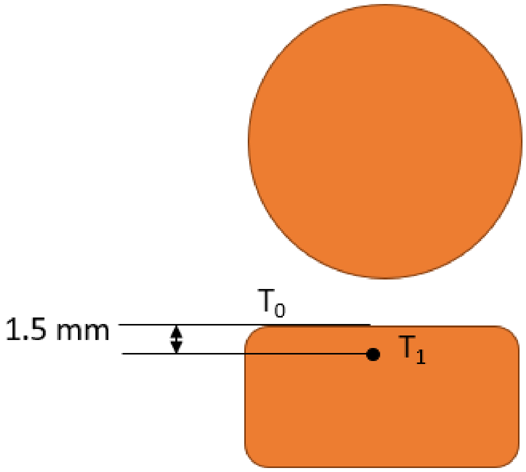

Figure 18. Test section - not to scale.

4.5. Methodology

A cartridge heater plate was connected to a power supply and kept below the test copper chip. A layer of thermal paste was applied to the connecting surface to have a thermally conductive layer in between and to avoid any air gap. The chip was provided with a hole on the side near the upper surface which was used to connect to the thermocouple for the measurement of the surface temperature. The heater supplies voltage across the cartridge heater, which is in contact with the copper chip. The copper chip gets heated due to conduction. The temperature is measured using a thermocouple. A needle connected to the syringe dispenses the liquid on the surface. As the surface is hot, the droplet evaporates, starts to recede, and interference patterns are seen. These interference patterns are recorded using the microscope and analyzed in MATLAB to calculate the thickness of the film.

4.6. Data Acquisition

The data acquisition from the setup was through two K- type thermocouples. One thermocouple was inserted into the test section at a distance of 2 mm from the top surface, which was the polished, smooth surface used for the testing. The second thermocouple was inserted in the meniscus and the temperature of the meniscus was captured. Both the thermocouples were inserted into a Fluke 52 II digital thermometer. The Kent Scientific syringe pump was interfaced with a LabVIEW program on a desktop and the flowrate was controlled manually. A video of the evaporating droplet and the evaporating meniscus was captured using two KEYENCE cameras. One of the optical cameras was in top view, illuminated by a red, coherent laser source and the second was from the side view illuminated by white light. These videos were processed in MATLAB to calculate the volume of the meniscus and thickness profile of the receding evaporating droplet.

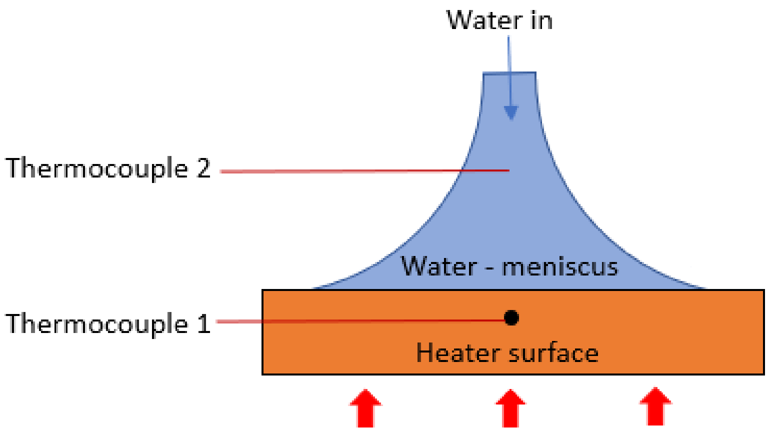

Figure 19. Positions of thermocouples for measurement of temperature of surface and meniscus.

4.7. Method to calculate the thickness of the film with MATLAB

A MATLAB program was developed to analyze the recorded videos and process them to find the thickness profile, micro-contact angle and contact line velocity of the receding and advancing contact line during the process of evaporation. The algorithm of the MATLAB program is as follows –

1. Set the variable values. Wavelength $\lambda$and refractive index of water, n_W (depending on water temperature), initial frame value, frame step. Where, n_W is the refractive index of water.
2. Open the initial frame as an image. Select the area in the image to enlarge where the fringes are clear.
3. Mark the black fringes, starting from the contact line in the direction of the center of the receding droplet. Press enter to end the frame sequence.
4. The program loops and opens the frame after skipping the number defined by the frame step.
5. This process is repeated until the droplet disappears or the fringes are no longer clear enough to be analyzed.
6. A thin pin of known thickness was kept under the microscope and measured to find the pixel to width ratio for all the distance calculations.

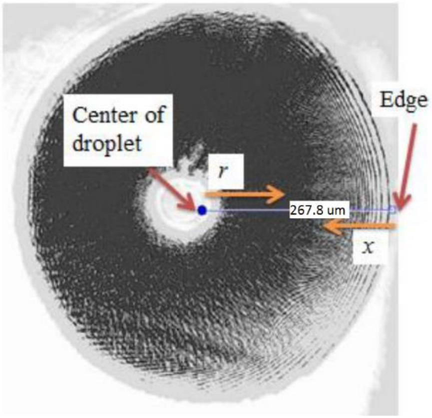

Figure 20. Droplet as seen through the optical lens.

Figure 20 shows the full view of a droplet on a copper surface. The image is in greyscale. The radius of the droplet is interpolated using a least square method, by plotting points on the circumference of the droplet. When zoomed in, only about a quarter of the droplet is visible on the screen, as shown in Figure 21(b). The schematic in Figure 21(a) shows an actual droplet and the area of the droplet visible on the screen.

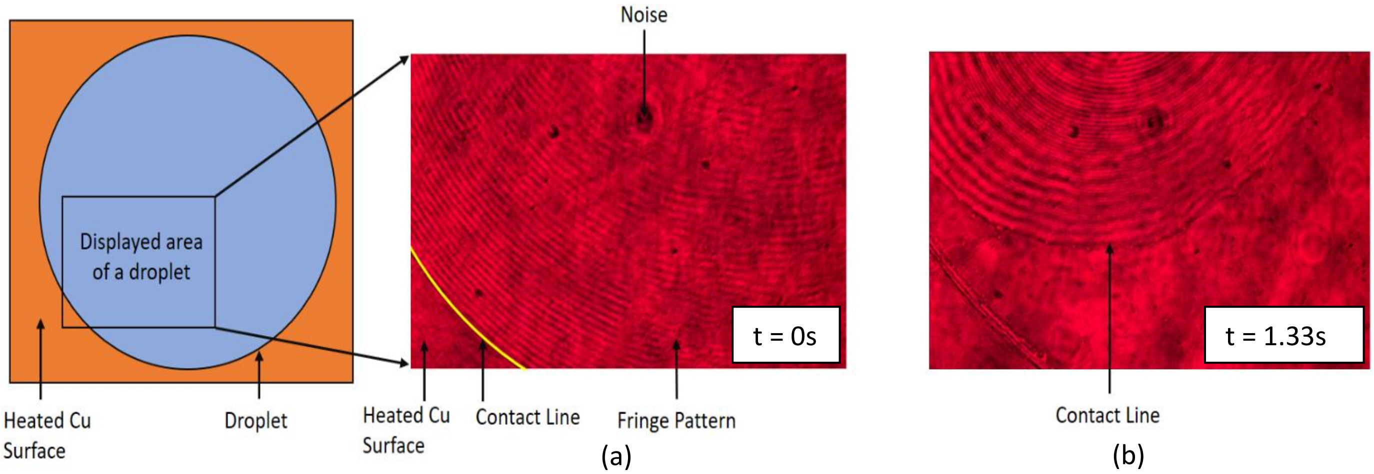

(a) (b)

Figure 21. (a) Area of the droplet seen on the screen. (b) Points marked on the contact line to interpolate the radius at t=0s.

At t = 0s, the position of the contact line is shown in Figure 21(a), while the position of contact line after t = 1.33s is shown in Figure 21(b). All the dark fringes are marked with points and thickness profile at that position is calculated using the equation -

$$2t = m\lambda \tag{12}$$

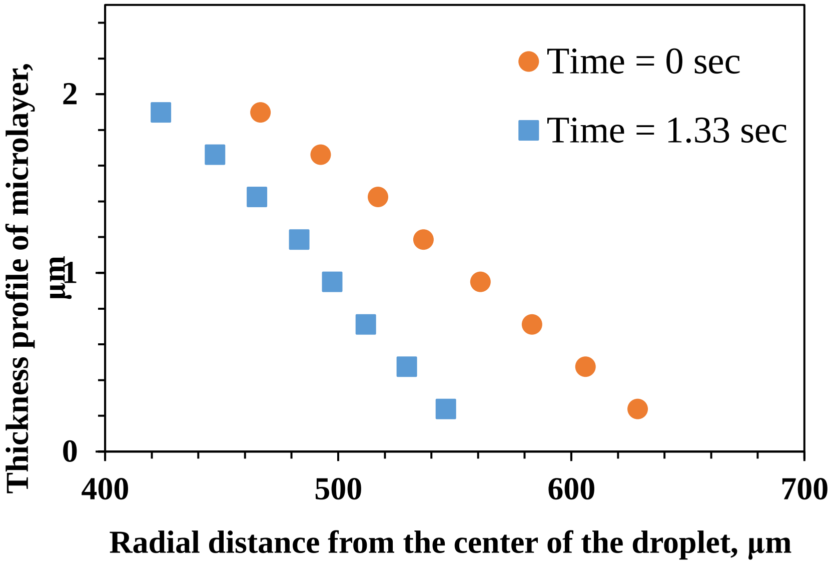

Figure 22. Thickness profile corresponding to Figure 15(a) and 15(b), for surface at 40°C.

Figure 22 shows the thickness profile corresponding to images shown in figure 21(a) and 21(b). For series t = 0 sec in the above plot, every marker point is a dark fringe at a distance from center of the droplet shown on x-axis. First marker is on the contact line and is farthest from center of the droplet. The center of droplet is estimated by marking points on the contact line using least square method.

The reduction in contact angle as seen between the series at time t = 0 sec and t =1.33 sec can be seen. This is seen as the contact line is pinned and thin film stretches and thins out even more.

4.8. Validation of Interferometry

A microscope slide of dimensions 25 mm x 75 mm placed on top of a silicon wafer of the same dimensions. A silicon wafer with a known thickness of 320 µm is then placed in between the slide and the silicon wafer to create an air gap as shown in the Figure 23. Hence, we obtain a triangle of the dimensions as 75 mm base (x) and 320µm as height (y). Due to the difference in the traveled distance of the optical rays AD and ray BC in Figure 3, bright and dark fringes of constant thickness are seen, which are equally spaced. As the thickness of the fringes is constant due to constant slope, the following equation gives the film thickness by marking the dark bands(m)-

$$t = \frac{m\lambda}{2n_w} \quad m = 1,3,5.. \tag{13}$$

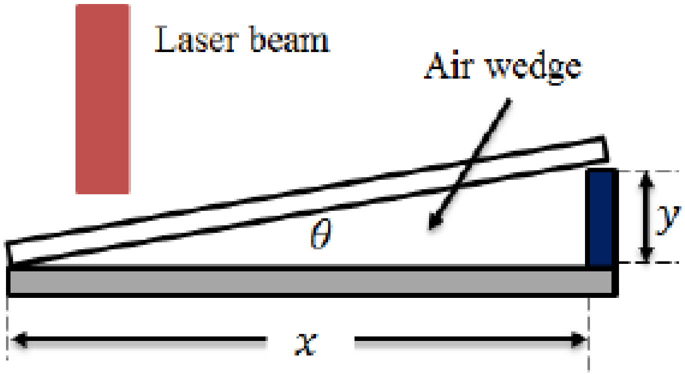

Figure 23. Experiment on air wedge for validation.

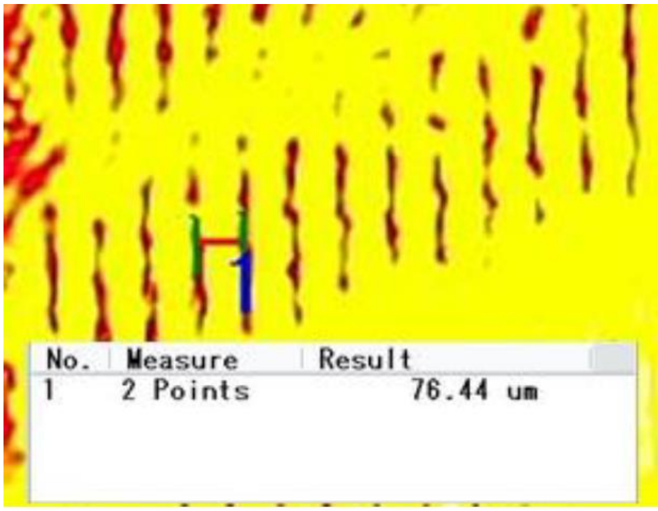

No.	Measure	Result
1	2 Points	76.44 um

Figure 24. Fringe spacing measurements.

This analytical result is compared with the fringe spacing obtained using the experimental setup.

The experimental result for film thickness is Δx_{exp} = 76.44µm. The discrepancy between the analytical and experimental approaches is given by:

$$\% Deviation = \left|\frac{\Delta x - \Delta x_{exp}}{\Delta x}\right| \times 100 = 3.07\% \tag{14}$$

The value of the deviation is low, and it can be concluded that the experimental approach used is capable of accurately predicting the thickness profile from interference patterns.

4.9. Uncertainty Analysis

The total uncertainty comprises of two parts; bias error and precision error:

$$\text{Total Uncertainty, } U = \sqrt{{U_b}^2 + {U_p}^2} \tag{14}$$

Bias error is the difference between expected measurement value and the true measurement value. So, bias errors are the errors due to calibration while precision errors are due to the sensitivity of the testing instruments.

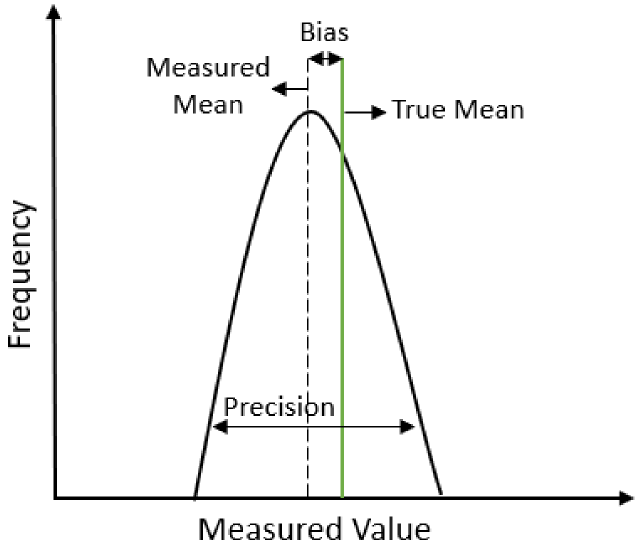

Figure 25 Bias and Precision uncertainties

In this experiment, it was important to understand the uncertainty associated with temperature and volumetric flow rate as the estimation of heat transfer is performed using these values. Thermocouple was calibrated in a hot cell at known temperatures and the thermocouple readings were noted. Bias uncertainty was calculated by obtaining the deviation of the resulting values from the preset values on hot cell and the values were used by calibrating using the equation. Precision uncertainty was calculated by repeating the experiment multiple times and calculating standard deviation of the results. The standard deviations were multiplied by 2 to account for 95% of the deviation. Total uncertainty was 0.1°C after the thermocouple was calibrated using the bias uncertainty.

$$\text{Bias Uncertainty} = 2 \times \sqrt{\frac{\sum(Obtained\ Value - True\ Value)^2}{Number\ of\ Values}} \tag{15}$$

$$\text{Precision Uncertainty} = 2 \times \sqrt{\frac{\sum(Obtained\ Value - Average\ of\ obtained\ values)^2}{Number\ of\ Values}} \tag{16}$$

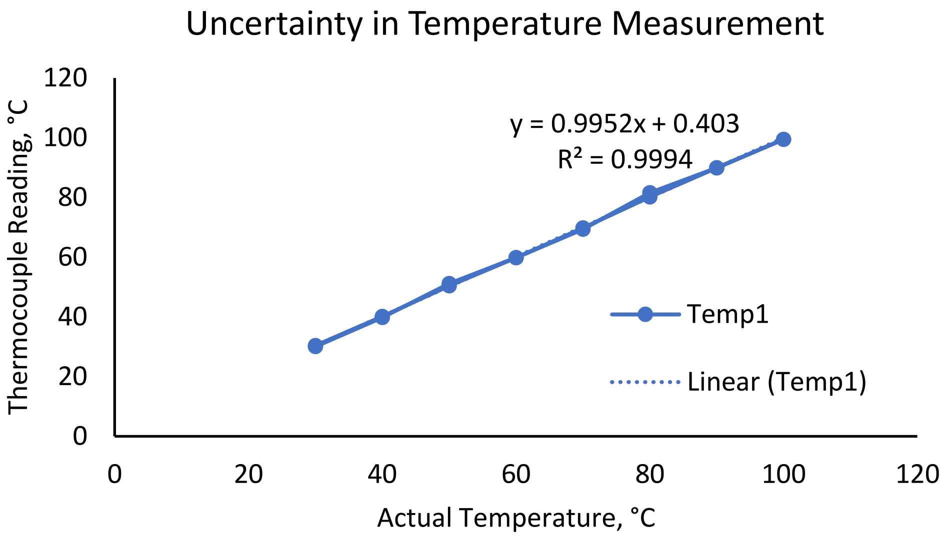

Figure 26 Bias uncertainty in thermocouple

Uncertainty measurement for flow rate was accomplished by applying the constant flow rate to the syringe pump for 20 minutes and initial and final position of the bore tip of syringe piston was marked by capturing images. These images were processed using high speed image analysis, and error was calculated for each flow rate. This was repeated 5 times for each flow rate. Same formulae and method to calculate uncertainty as described for thermocouple was used while calculating the volumetric flow rate uncertainty. The uncertainty was observed to be 10% at the lowest flow rate and reduced as the flow rate increased.

Mass flow rate was calculated using the density.

$$\dot{m} = \rho \dot{V} \tag{17}$$

Propagation of volumetric flow uncertainty in mass flow rate was calculated using the following equation –

$$U_{\dot{m}} = \sqrt{\sum_{i=1}^{n} \left(\frac{\partial \dot{m}}{\partial \sigma_i} U_{\sigma_i} \right)^2} \tag{18}$$

$$\frac{U_{\dot{m}}}{\dot{m}} = \sqrt{\frac{\left(\frac{\partial \dot{m}}{\partial \rho} U_\rho \right)^2 + \left(\frac{\partial \dot{m}}{\partial \dot{V}} U_{\dot{V}} \right)^2}{\dot{m}^2}} \tag{19}$$

The uncertainty for the density (U_ρ) was evaluated by calculating the change in density values at temperature values including the uncertainty.

$$U_\rho = \left| \rho_T \pm \rho_{T \pm U_T} \right| \tag{20}$$

The expressions are then rewritten in terms of the function of interest, $\dot{m}$

$$\frac{\partial \dot{m}}{\partial \rho} = \dot{V} = \frac{\dot{m}}{\rho} \tag{21}$$

$$\frac{\partial \dot{m}}{\partial \dot{V}} = \rho = \frac{\dot{m}}{\dot{V}} \tag{22}$$

These equations are substituted in (19)

$$\frac{U_{\dot{m}}}{\dot{m}} = \sqrt{\frac{\left(\frac{\dot{m}}{\rho}U_{\rho}\right)^2 + \left(\frac{\dot{m}}{\dot{V}}U_{\dot{V}}\right)^2}{\dot{m}^2}} = \sqrt{\frac{\frac{\dot{m}^2}{\rho^2}U_{\rho}^2 + \frac{\dot{m}^2}{\dot{V}^2}U_{\dot{V}}^2}{\dot{m}^2}} \qquad (23)$$

$$\frac{U_{\dot{m}}}{\dot{m}} = \sqrt{\frac{U_{\rho}^2}{\rho^2} + \frac{U_{\dot{V}}^2}{\dot{V}^2}} \qquad (24)$$

Using the uncertainty in $\dot{m}$, the uncertainty in heat transfer rate was calculated. Heat transfer rate can be caluclated using following equation –

$$q = \dot{m}h_{fg} \qquad (25)$$

$$U_q = \sqrt{(\dot{m}U_{h_{fg}})^2 + (h_{fg}U_{\dot{m}})^2} \qquad (26)$$

The uncertainty in h_{fg} i.e. ($U_{h_{fg}}$) was calculated using the uncertainty in temperature measurement by evaluating the change in h_{fg} values at temperatures including uncertainties.

$$\frac{U_q}{q} = \sqrt{\frac{{U_{h_{fg}}}^2}{{h_{fg}}^2} + \frac{{U_{\dot{m}}}^2}{\dot{m}^2}} \qquad (27)$$

For all the values, uncertainty calculated for heat transfer was less than 10%.

5. Results

The thickness profile of an evaporating droplet was analyzed using the mentioned MATLAB program. Micro-contact angle, contact line velocity was calculated using the thickness profile and the displacement of the contact line with time, respectively.

Advancing and Receding contact angle and Surface Roughness for all the tests -

The surface was polished to under 1 µm roughness and a laser confocal microscope was used to measure the surface roughness. A goniometer was used to measure the advancing and receding contact angles of distilled water on the polished copper surface. The advancing and receding angles were found to be 85.3° and 20.2° respectively. The average surface roughness of the surface was 0.18 µm.

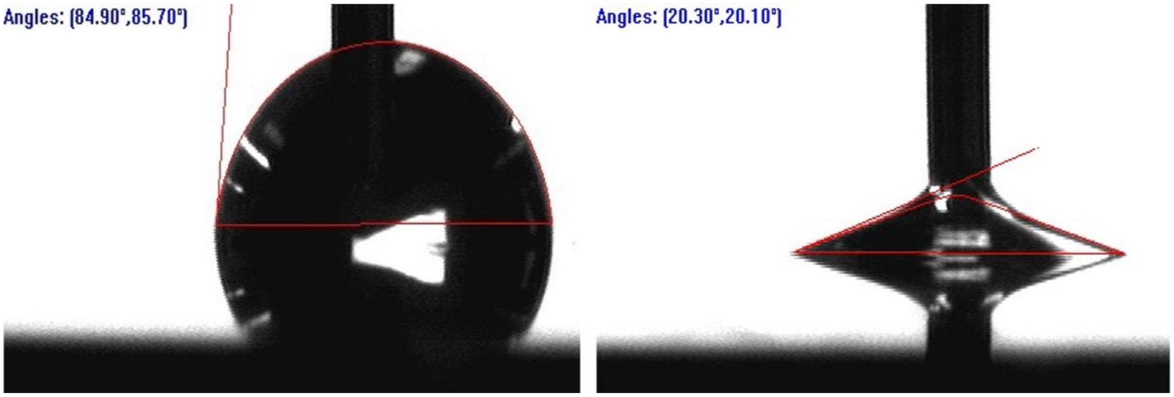

Figure 27. Advancing and Receding contact angle on polished copper surface.

5.1. Thickness Profile of Thin Film Evaporation at Various Temperatures

A droplet of volume 2 µL was dispensed using the dispensing pump on the heated surface. The droplet takes a semi-circular cap shape and the contact line is pinned. Height of the droplet reduces until a certain critical value at which the Young's forces are imbalanced. At this point, the contact line starts to recede, and the height remains at a similar value. The videos were captured when the contact line started to recede. Figure 28 shows the process of evaporation of a droplet.

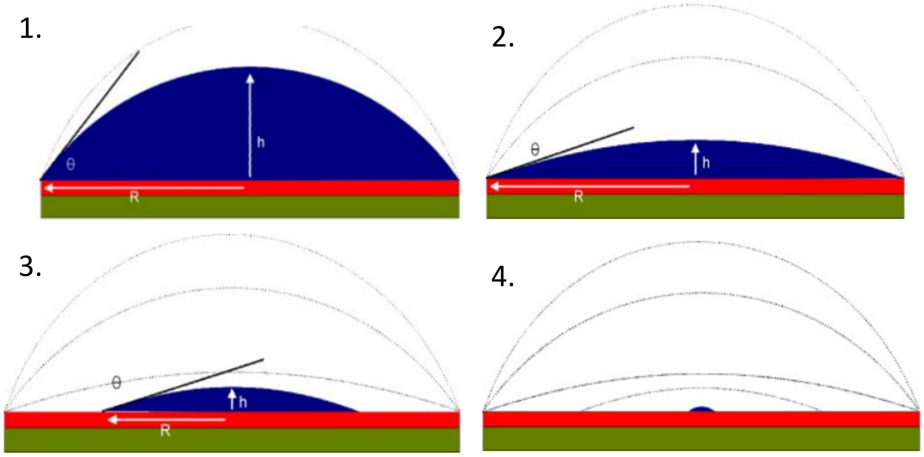

Figure 28. Four stages of drop evaporation.

Figure 29 shows the receding contact line on a heated copper surface at frame no. a)F = 0, b)F= 140, c)F = 252.

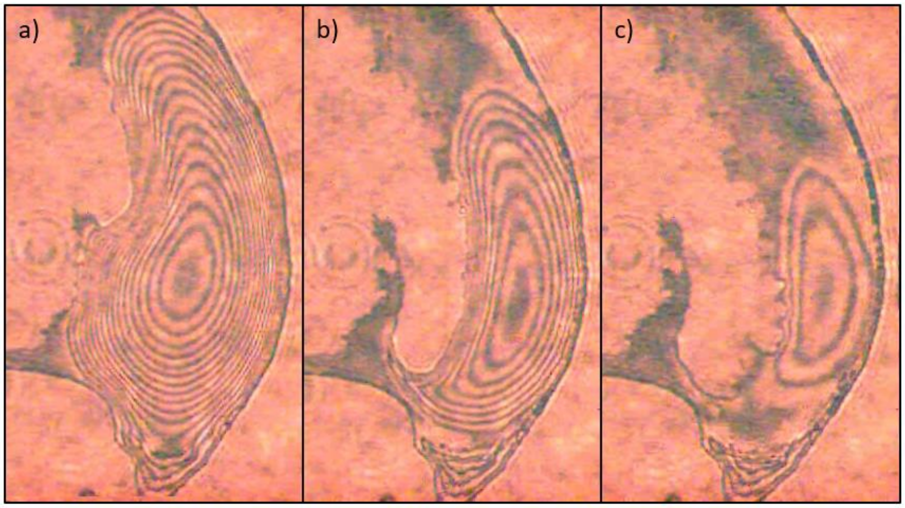

Figure 29. Evaporation of thin film a = frame 0, b = frame 140, c = frame 252.

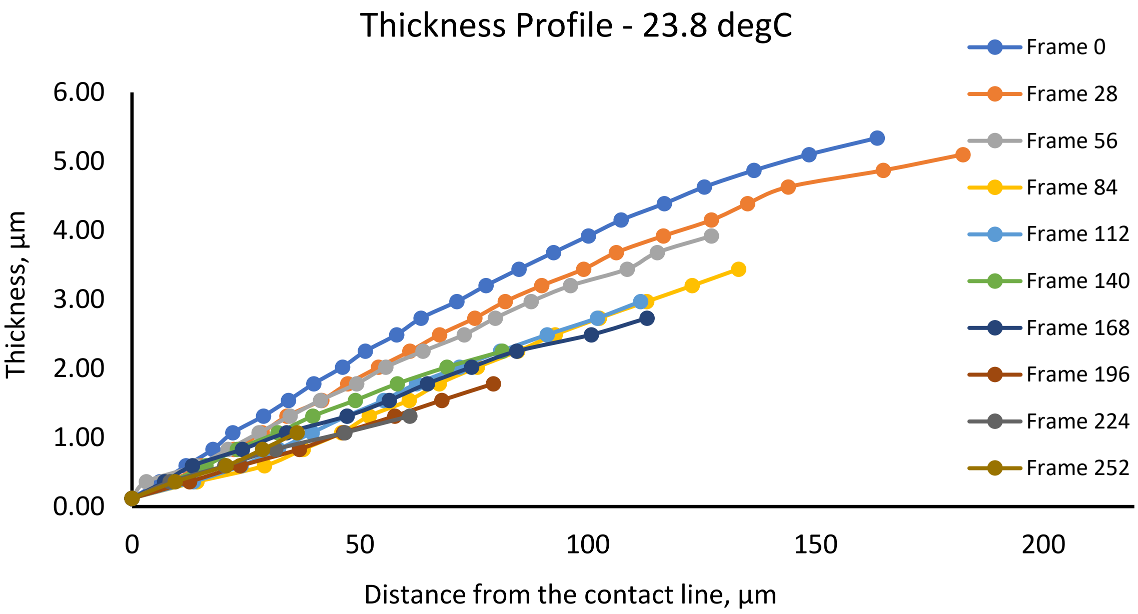

Figure 30. Thickness profile of an evaporating thin film at 23.8 °C corresponding to figure 29.

The contact angle during the evaporation cycle reduces towards the end of the drop life. This is indicative of thinning and stretching of the film. Similar plots were achieved for temperatures between 23 °C to 70 °C .

Table 2 Comparison of thickness profiles from the literature.

Author	Working Fluid	Contact Angle	Max Measured Thickness
Satbyoul Jung & Hyungdae Kim[53]	Di water on ITO film	0.25°	3.3 µm
Ming Gao, Lixin Zhang, Ping Cheng, Xiaojun Quan[20]	Ethanol on ITO film	2.24°	4 µm
Hyungdae Kim, Jacopo Buongiorno[54]	Di Water on Si wafer	0.30°	3.5 µm
Zhihao Chen, Atsushi Haginiwa, Yoshio Utaka[25]	Di water on Quartz	0.75°	5.5 µm
Present Study	Di Water on polished Cu	1.70°	5.5 µm

In the literature almost all the studies are done with a pool boiling setup with an artificial nucleation site on the heater surface. In such cases, the heater surface is often transparent to light and is projected from bottom of the surface as shown in Figure 9. In this study, the optical camera and the laser source both were above the opaque surface. The surface used as heater surface was a polished copper surface. From Table 2, we can see that the values obtained are comparable to the data published in the literature. Hence, with this method we can use opaque, mirror finished surfaces to study the microlayer properties of liquids and the interactions of liquid with the heater surfaces.

5.2. Contact Line Velocity and Contact Angle vs Surface Temperature

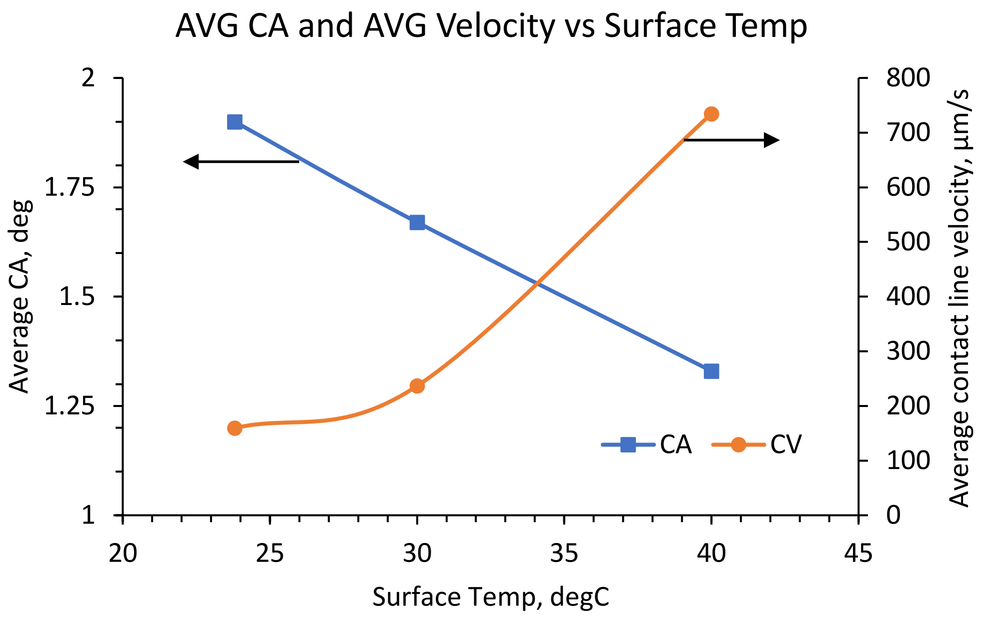

Figure 31. Average contact angle (AVG CA) and average contact line velocity in an evaporating thin film.

The micro-contact angle and the contact line velocity was plotted against the surface temperature. The contact angle tends to decrease with increase in the temperature while the contact line velocity increases sharply as the temperature of the heater surface increases.

5.3. Conversion of Partial Pressure to Wall Superheat

To account for the humidity in testing of static and oscillating meniscus a wall super heat value was calculated on the basis of humidity percentage and ambient temperature. To calculate the saturation temperature of water at the partial pressure conditions, a psychrometric chart was referred. The relative humidity was recorded during all the experiments and this was converted into wall superheat by subtracting the saturation temperature from the surface temperature.

$$T_d = T - \frac{100 - RH}{5} \tag{28}$$

where, T_d is the dew point temperature, T is the air temperature and RH is the relative humidity. At the dew point temperature, the air is saturated and therefore we can write,

$$T_d = T_{sat} \tag{29}$$

Therefore, wall superheat

$$\Delta T = T_{wall} - T_{sat} \tag{30}$$

5.4. Evaporation of Static and Oscillating Meniscus

The evaporation rate of an oscillating meniscus was analyzed. Meniscus was imparted with a frequency of 0 Hz, 0.6 Hz, 1.2 Hz, 1.8 Hz and 2.4 Hz. The meniscus associated with 0 Hz frequency does not oscillate and is termed as a static meniscus.

A meniscus was formed as shown in Figure 32 and a constant flow rate was imparted such that the volume of the meniscus remained constant with time. Volume of the meniscus was calculated using volume of revolution by measuring the height, radius and estimating a second-degree polynomial for the outer curve.

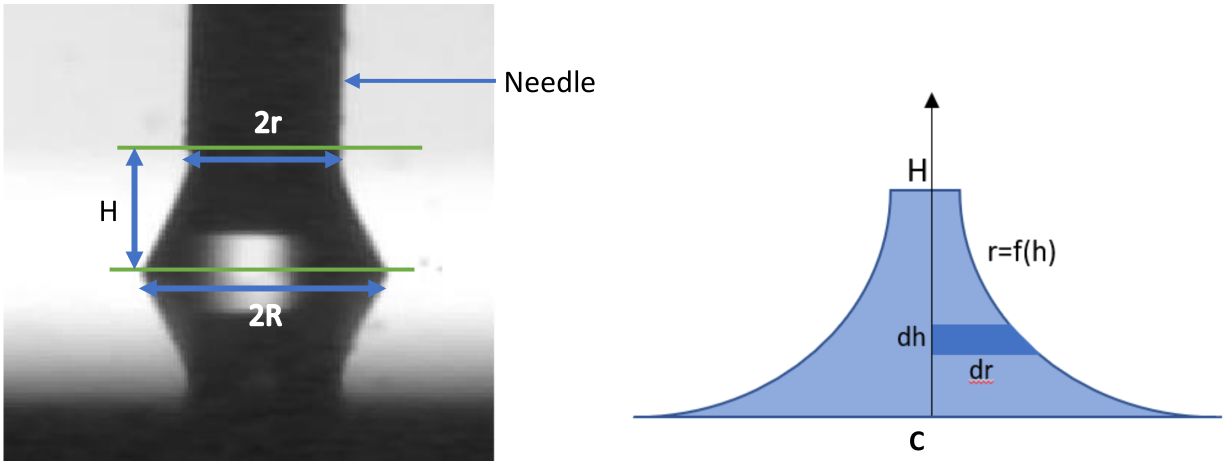

Figure 32. Static meniscus from side view and Volume of Revolution

The equation for volume of revolution is –

$$\int_{C}^{H} \pi r^2 \, dh \tag{31}$$

$$\int_{C}^{H} \pi (ah^2 + bh + h)^2 \, dh \tag{32}$$

5.5. Volume of Static meniscus Over Time

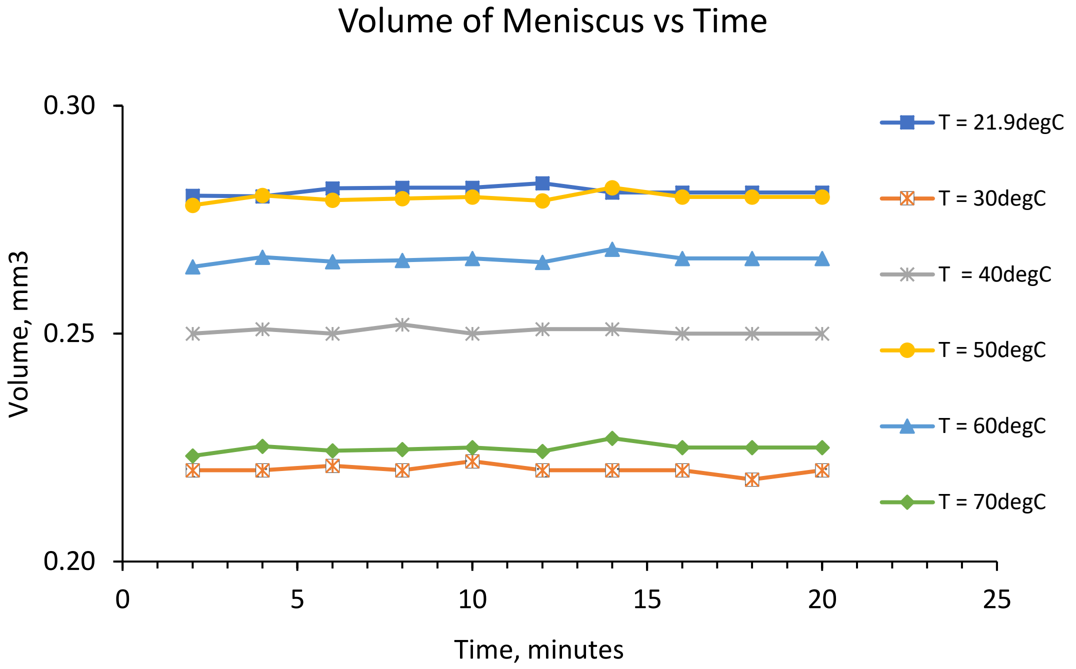

Figure 33. Volume of static meniscus over time.

As the volume of the evaporating meniscus was constant with a constant flow rate of water, the evaporation rate can be calculated.

$$\dot{v} = \rho \dot{m} \tag{33}$$

Total heat flow can be calculated using the following equation –

$$q = \dot{m} h_{fg} + \dot{m} c_p$$

(34)

where, $\dot{v}$= volumetric flow rate in m^3/s, ρ = density of distilled water in kg/ m^3, $\dot{m}$ = mass flow rate in kg/s.

5.6. Oscillating Meniscus Volume

The volume of the oscillating meniscus is calculated and plotted over time in the same way as in the case of the static meniscus. For the oscillating meniscus, the minimum position of the meniscus was chosen to calculate the volume using volume of revolution. Figure 34 shows the minimum and maximum position of the meniscus. The volume change over time was recorded for all frequencies.

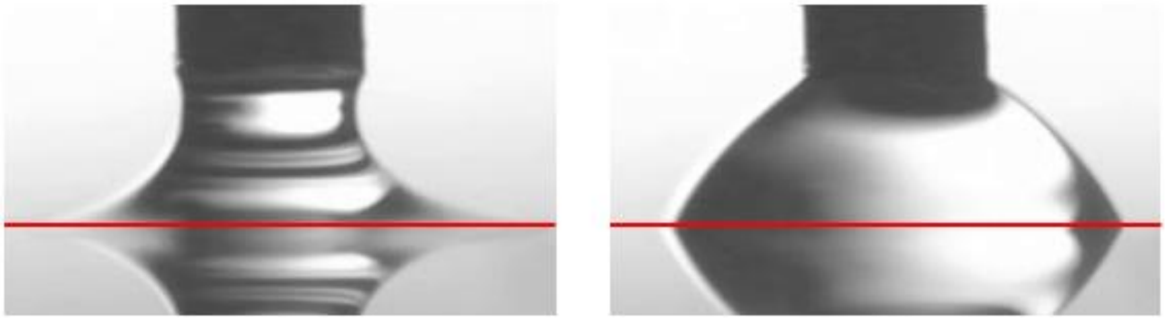

Figure 34. Minimum and maximum positions in an oscillating meniscus.

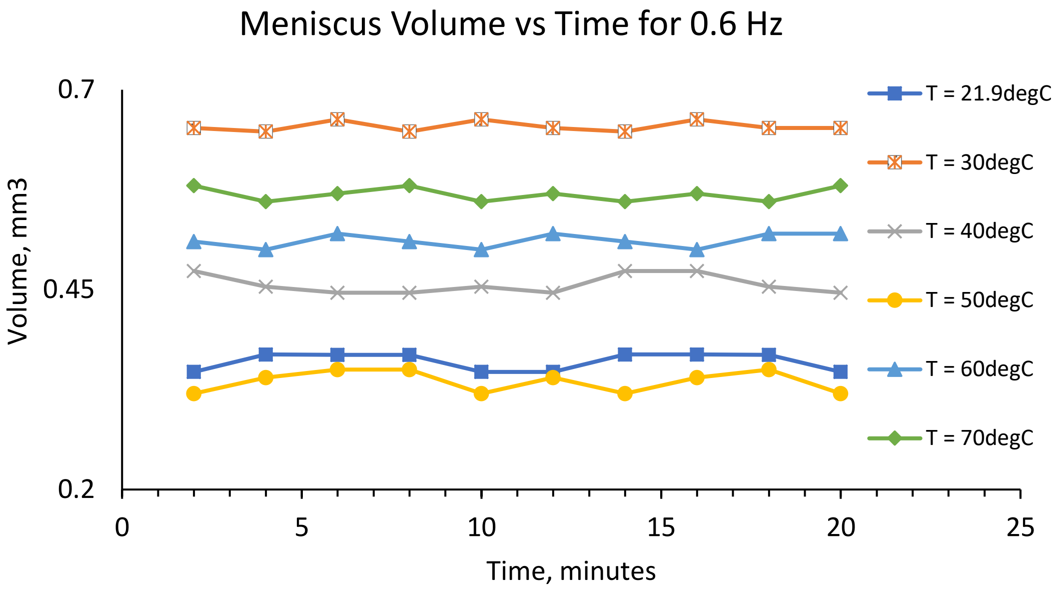

Figure 35. Meniscus volume at minimum position of an oscillating meniscus at 0.6 Hz frequency.

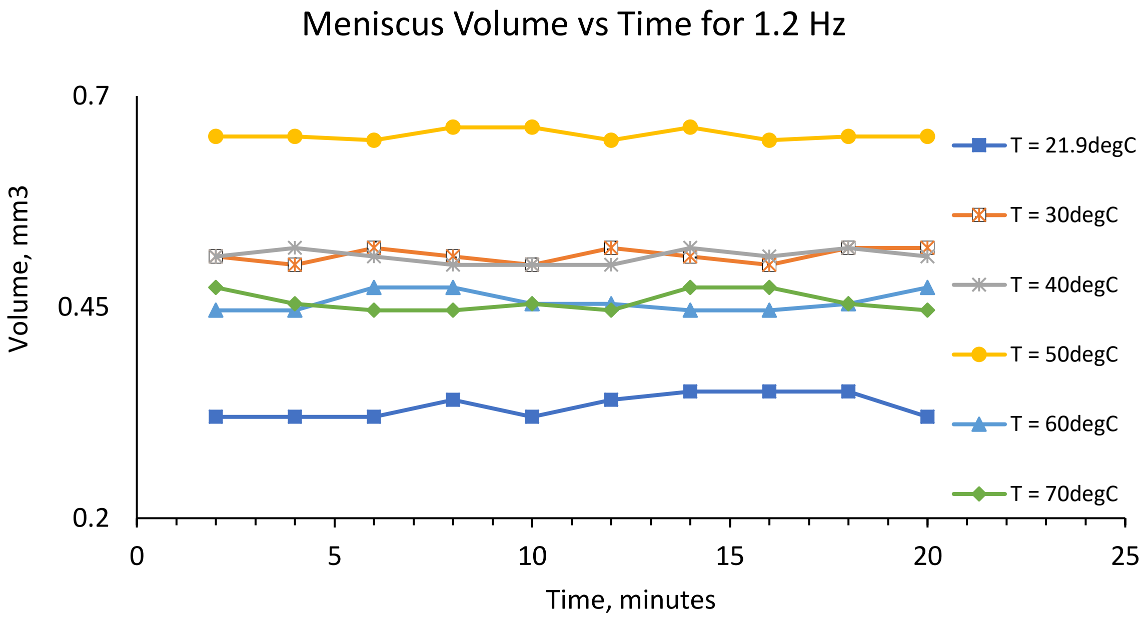

Figure 36 Meniscus volume at minimum position of an oscillating meniscus at 0.6 Hz frequency

5.7. Calculation for determining Heat Transfer Coefficient

Assuming meniscus is a cylinder of uniform temperature equal to the surface temperature. Heat transfer to the cylinder tip is assumed negligible.

Properties –

Diameter, D = Average of smaller and larger diameter in mm

Static meniscus, Air velocity in room, V = 0.01 m/s – natural convection

Thermal conductivity, k = 26.3 x 10^{-3} W/m-C

Kinematic Viscosity, ν = 15.89 x 10^{-6} m^2/s

Prandtl Number, Pr = 0.707

Prandtl Number at water temperature, Pr_s = 0.705

Using Zukauskas relation -

$$Nu = CRe_D^m Pr^n \left(\frac{Pr}{Pr_s}\right)^{\frac{1}{4}} \tag{35}$$

Since Pr < 10, n = 0.37

Table 3 Constants of Nusselt Number equation for circular cylinder cross flow – Zukauskas relation

Re_D	C	m
1 - 40	0.75	0.4

$$Re_D = \frac{VD}{\nu} \tag{36}$$

$$h = Nu_D \frac{k}{D} \tag{37}$$

H is generally in the range 5 to 100 for such applications. H is sensitive to the air velocity $h \propto V^m$

5.8. Heat transfer through Surface Area and Contact Line of meniscus

Mass transfer rate through the surface area of the meniscus was calculated using the following equations –

$$\dot{m} = h_D \left(W_{s,w} - W_{air}\right) \times Area \tag{38}$$

$W_{s,w}$ is humidity ratio of saturated water and W_{air} is the humidity ratio of air.

From Lewis relation, assuming Lewis number = 1,

$$h_D = \frac{h}{cp_m} \tag{39}$$

Where, $\dot{m}$ is the mass transfer rate (kg/m^2-s), h_D is the diffusion coefficient (kg/m^2-s) and cp_m is specific heat at film temperature (kJ/kg°C) .

$$W_{s,w} = 0.622 \times \frac{P_{w,s}}{P - P_{w,s}} \tag{40}$$

$$C_p = C_{p,a} + C_{pw} W_m \tag{41}$$

C_p is specific heat at mean humidity ratio, $C_{p,a}$ is specific heat of air and C_{pw} is specific heat of water.

As observed by Raghupathi and Kandlikar[55] and Kandlikar et. al.[56] that increasing the contact line length by adding microgrooves on a plane and tubular surface increased the wetted surface area CHF by 1.5 times. They claimed that additional contact line around microgrooves act as a reservoir to supply liquid to the evaporating microlayer in the contact line region of an evaporating bubble in pool boiling. Present study calculates the contribution of heat transfer in the contact line region of an evaporating meniscus which is similar to a region between two evaporating bubbles as shown in figure 8.

Heat transferred through the surface area of the meniscus from convection can be compared against the heat transfer through the contact line by subtracting the calculated total $\dot{m}$ from equation 38 and subtracting it from the total mass coming in the system(equation 34). Total mass flowing into the system is known from the rate of flow of water through the syringe dispenser. Heat transfer rates were calculated and plotted for HTC(h) = 10 W/m^2°C and 20 W/m^2°C as these values of HTC give a good range of heat transfer values. It was found that contribution of contact line heat transfer was approximately 96% - 85% and 4% - 85% heat was transferred through the surface of the meniscus for h = 10 W/m^2°C and contribution from contact line was 82%-55% and 18%-45% from the surface of the meniscus for h = 20 W/m^2°C.

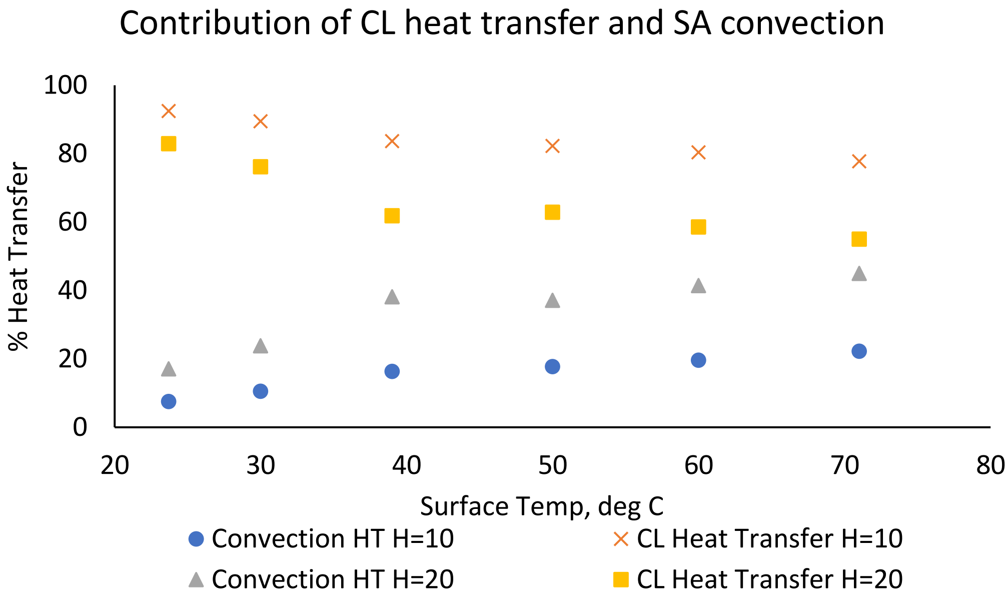

Figure 37 Percent Heat transfer through Surface Area (SA) of meniscus and Contac Line (CL) region, H in W/m^2°C

5.9. Heat Flux vs. Wall Superheat and Effect of Diameter – Static Meniscus

When contact line heat transfer values were plotted for different diameters, it was observed that as the surface temperature went up, the evaporation rate increases and hence the flow rate of the water coming into the meniscus increases. A test was done to analyze the effect of the footprint area of the meniscus. Three base - diameters were tested at each temperature.

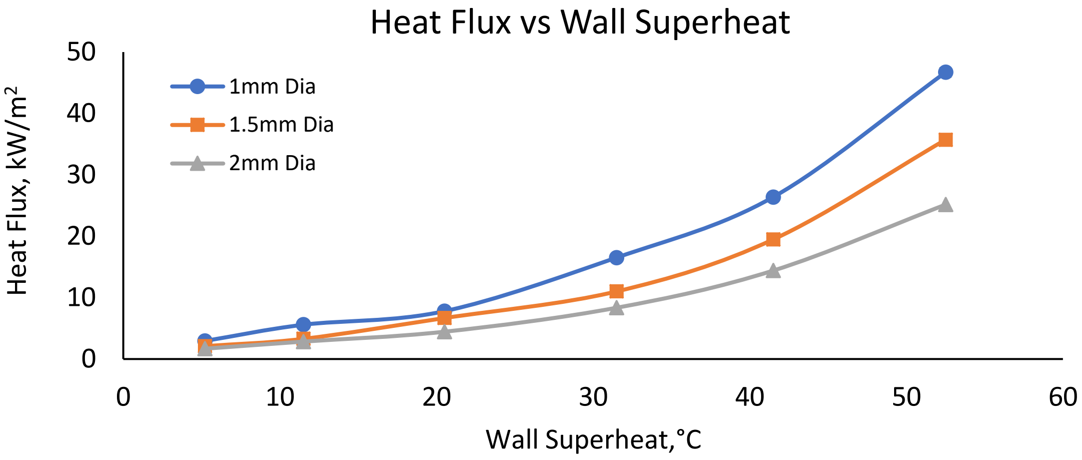

Figure 38. Effect of diameter on heat flux vs wall superheat.

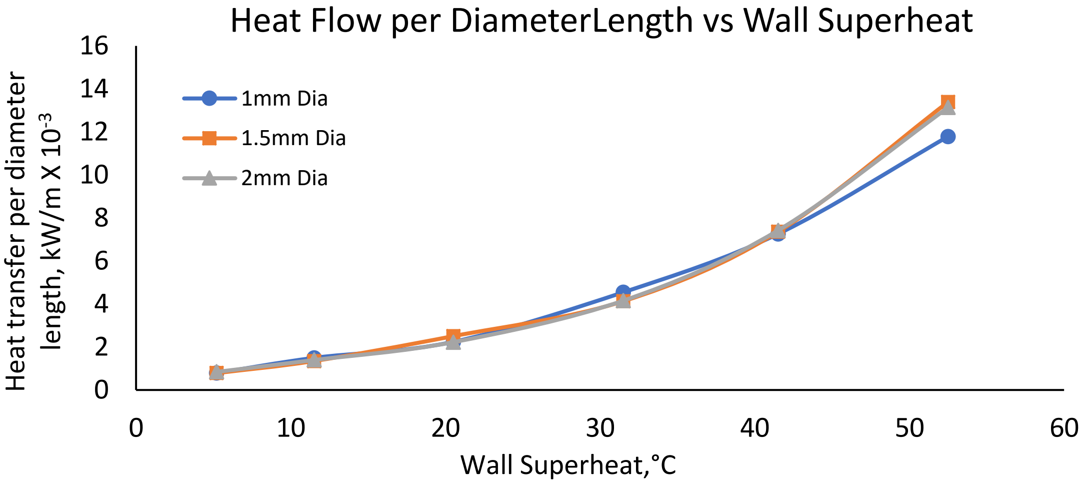

Figure 39. Circumferential heat transfer vs wall superheat.

From the Figures 38 and 39, we can see that though the heat flux increases with an increasing surface temperature and decreasing diameter, the heat per diameter length is constant at any given temperature for a stable meniscus.

5.10. Effect of Frequency on Oscillating Meniscus

The oscillating meniscus was imparted four frequencies – 0.6 Hz, 1.2 Hz, 1.8 Hz and 2.4 Hz. It is clear from the Figure 40 that as the frequency of oscillations is increased, the heat transfer rate per unit base length for all the curves – coincide. This shows that the contact line heat transfer per unit length of the contact line is constant for all frequencies at given temperature at of the surface.

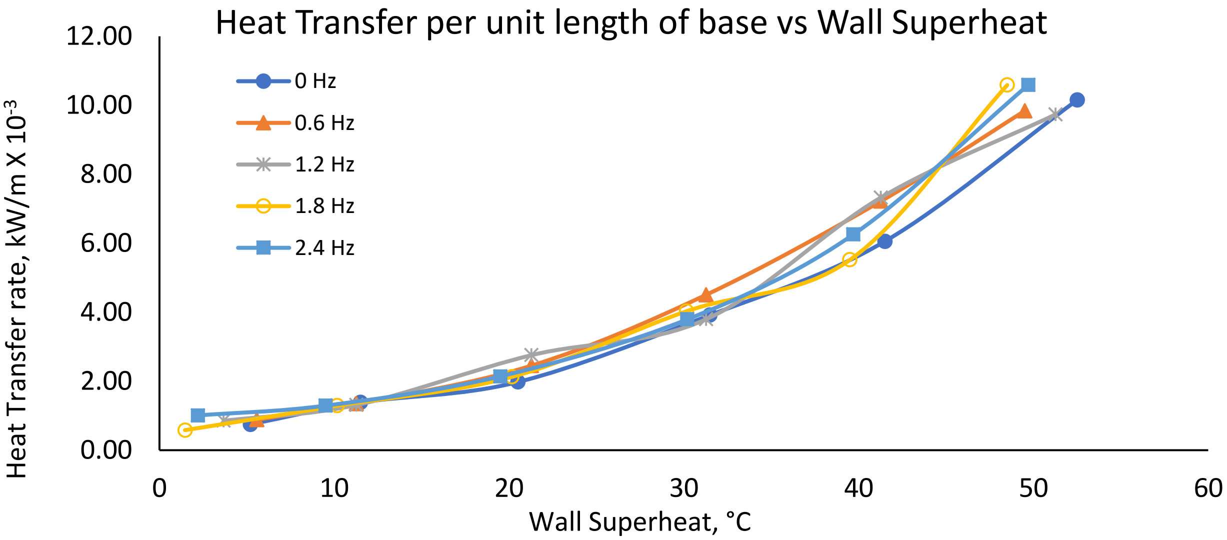

Figure 40 Heat transfer per base length for various frequencies and effect of contact angle on the heat transfer per unit base length.

5.11. Characteristics of Microlayer in an Oscillating Meniscus

As the meniscus oscillates, it thins out near the contact line area due to being pinned. The variation in the thickness of microlayer was captured at 250 frames/second and over one oscillation cycle. A similar profile was observed for meniscus oscillating at 1.2 Hz. It was difficult to achieve a steady meniscus at higher frequencies of 1.8 Hz and 2.4 Hz that thinned out enough to produce a microlayer. The slope of the thickness profile was calculated, and this gave the variation in contact angle values of the microlayer corresponding to Figure 41. As the bulk liquid recedes, the contact angle decreases at first and then when the bulk liquid starts to flow in the microlayer, the contact angle increases. This is shown in Figure 43.

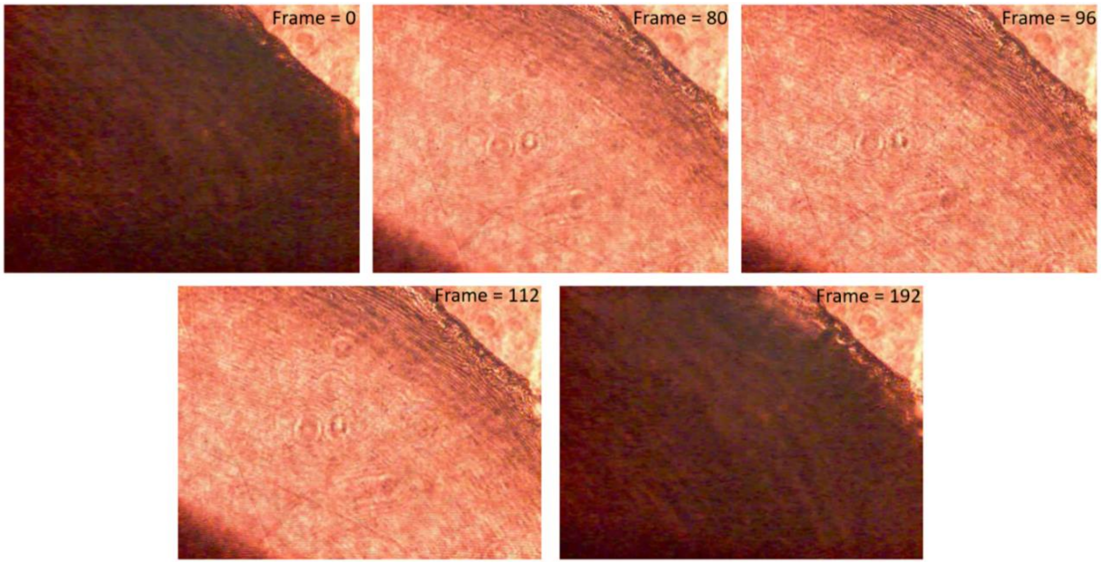

Figure 41. Evolution of microlayer in an oscillating meniscus.

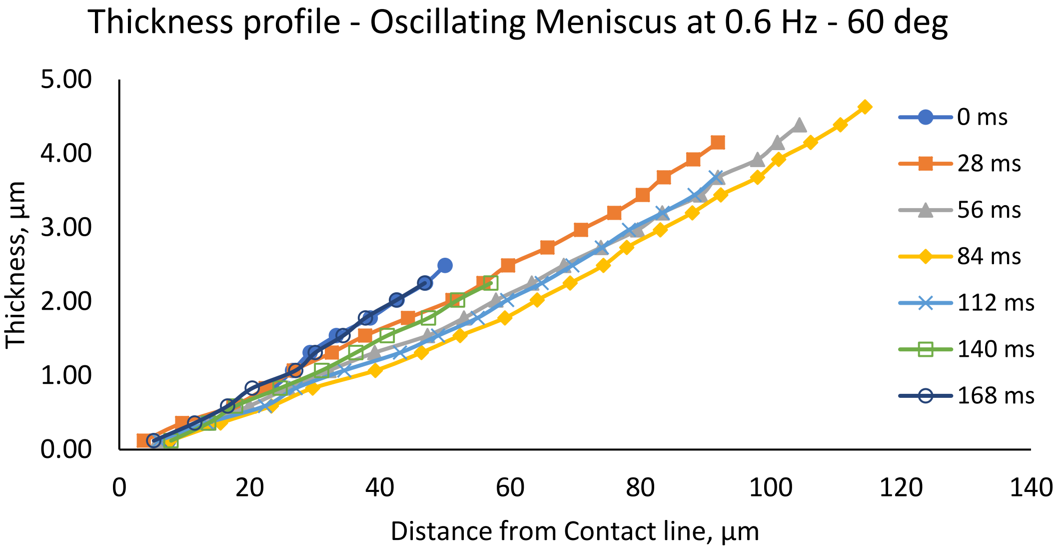

Figure 42. Thickness profile of microlayer formed in an oscillating meniscus at 60 °C – 0.6 Hz.

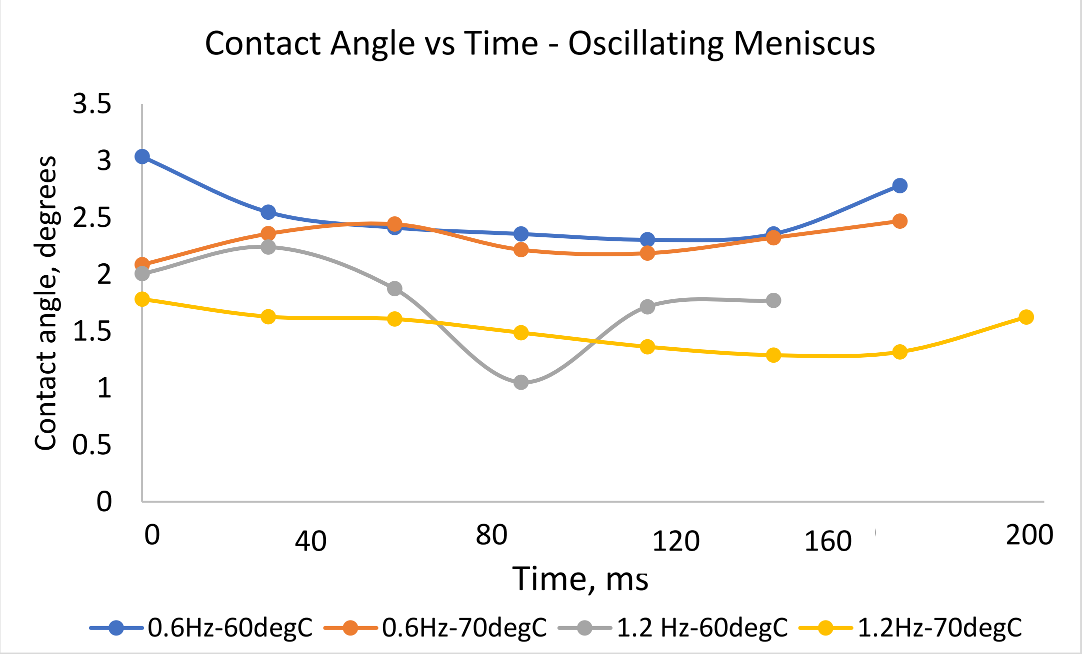

Figure 43. Variation of micro contact angle in the microlayer of an oscillating meniscus in one frequency.

At lower temperatures, there was no pinning of the contact line and hence no microlayer was observed. The contact line moved back and forth with the oscillations as shown in Figure 44.

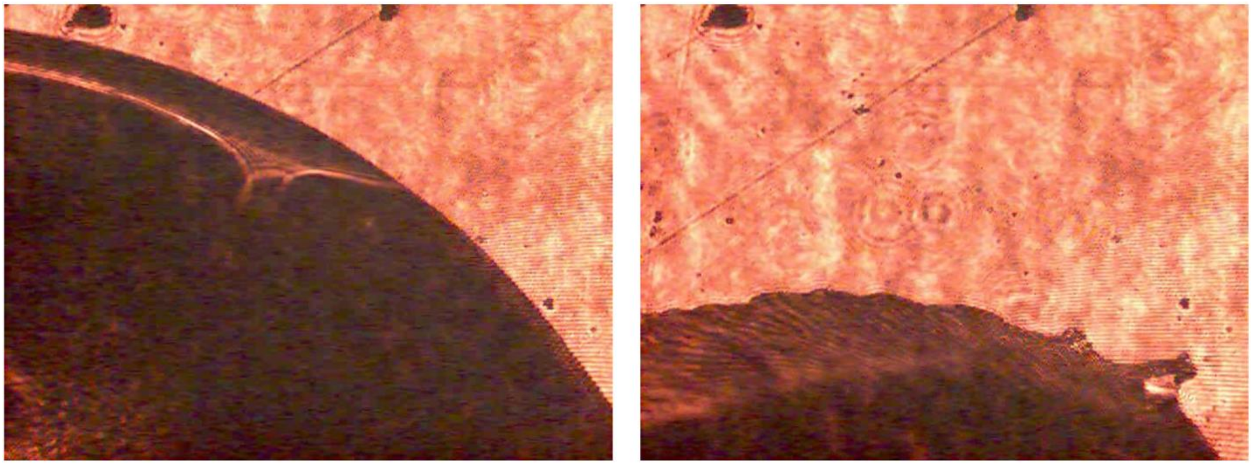

Figure 44. Maximum and minimum position of contact line at t = 0s and t = 0.6s - 0.6 Hz, 30 °C.

6. Conclusion

Tests were conducted on a polished, heated copper chip with roughness less than 1 μm to analyze the microlayer and contact line heat transfer of distilled water in an open-air system. Multiple tests were conducted like sessile droplet evaporation and static meniscus evaporation. A system was designed and fabricated to impart oscillations to the meniscus to understand the effects of oscillations and contact angle to an evaporating steady meniscus of DI water on the copper heater surface.

1. A system was designed and manufactured to form a steady and oscillating meniscus using a stepper motor and piston in a syringe.
2. This system was combined with the existing interferometry system to analyze the microlayer in the contact line area of the meniscus.
3. Sessile drop evaporation was observed under a red laser of wavelength λ = 632.8 nm under an optical lens at temperatures of surface varying from ambient to 70 °C. The droplet reduces in height and a thin film evaporation is seen with a thickness measured using the concept of interferometry. The fringe patterns at higher temperatures were not clear due to rapid motion of the receding contact line.
4. The micro, dynamic contact angle of the thin film was recorded along with the thickness profile and the receding velocity of the contact line. It was observed that as the surface temperature increased, the average contact angle value over the life of the thin film tends to increase. The velocity of the contact line increased sharply with an increase in surface temperature as well. The thickness values ranged from 0 to 5.5 μm.

5. Static and oscillating meniscus were tested. Meniscus was fed water at a rate constant to the evaporation to keep the net volume of the meniscus constant.
6. It was observed that the heat transfer per unit base area of the meniscus went down with increase in the diameter while the heat transfer per unit length of base of the meniscus was constant for a given temperature, humidity and varied diameters of the meniscus.
7. The contribution of contact line heat transfer was approximated by theoretical predictions to be around 96%-85% and the heat transferred from the surface was around 4%-15% for heat transfer coefficient of 10 $W/m^2°C$ and the contribution of contact line heat transfer was 82%-55% and contribution of convective heat transfer was 18%-45% for a heat transfer coefficient of 20 $W/m^2°C$.
8. The effect of frequency was analyzed on the rate of evaporation of a static and oscillating meniscus and it was found that frequency had negligible effects on the heat transfer per unit base length of the evaporating meniscus.
9. The microlayer formed in the contact line area of the oscillating meniscus was analyzed and the thickness values were calculated. The thickness values were in the range 0 to 5.5 µm.
10. Variation in micro contact angle was recorded using the thickness profile of the microlayer in oscillating meniscus.

7. Future Work

A test setup was put together in this experiment to obtain the contribution of heat transfer through the contact line of the meniscus and characteristics of a microlayer in an evaporating droplet and in the contact line region of the meniscus on a highly polished and heated copper surface.

It will be interesting to see the results with improvements in the test setup by keeping it under a controlled atmosphere. A glass cube can be incorporated which can have a controlled environment parameter like humidity, temperature and a cleaner air like argon gas inside the cube. Such controlled condition cubes are called environment chambers.

An array of thermocouples can be used instead of the copper surface to accurately measure the heat transfer rates over the complete oscillation cycle. This will allow the measurement of the change in temperature of the surface during the receding and the advancing stage of the contact line.

An infrared camera can be used on an infrared transparent surface to estimate the heat flux around the contact line area and measure the change in temperatures in a way similar to the proposed array of thermocouples.

The variation in the flow rate is sensitive to the temperature of the surface, and the sensitivity increases with increase in the temperature. To get even more accurate results the temperature of the surface can be controlled with a feedback loop connected to the supply and the joule heated cartridge. A comparison with different surfaces and different fluids like ethanol will help understand the topic better.

Tests surfaces can be varied and other surfaces like – Hydrophilic, hydrophobic, transparent surfaces with film heating can be adopted to view the thickness from bottom of the surface at higher temperatures.

References

[1] Yuan, Y., and Lee, T. R., 2013, “Contact Angle and Wetting Properties,” *Surface Science Techniques*, G. Bracco, and B. Holst, eds., Springer Berlin Heidelberg, Berlin, Heidelberg, pp. 3–34.

[2] Gao, L., and McCarthy, T. J., 2006, “Contact Angle Hysteresis Explained,” Langmuir, **22**(14), pp. 6234–6237.

[3] Panchamgam, S. S., Chatterjee, A., Plawsky, J. L., and Wayner, P. C., 2008, “Comprehensive Experimental and Theoretical Study of Fluid Flow and Heat Transfer in a Microscopic Evaporating Meniscus in a Miniature Heat Exchanger,” Int. J. Heat Mass Transf., **51**(21–22), pp. 5368–5379.

[4] Stephan, P., and Hammer, J., 1994, “A New Model for Nucleate Boiling Heat Transfer,” Heat Mass Transf., **30**(2), pp. 119–125.

[5] Snyder, N. R., and Edwards, D. K., 1956, “Summary of Conference on Bubble Dynamics and Boiling Heat Transfer,” Jet Propuls. Lab Pasadena Memo, (20–137).

[6] Cooper, M. G., and Lloyd, A. J. P., 1969, “The Microlayer in Nucleate Pool Boiling,” Int. J. Heat Mass Transf., **12**(8), pp. 895–913.

[7] Demiray, F., and Kim, J., 2004, “Microscale Heat Transfer Measurements during Pool Boiling of FC-72: Effect of Subcooling,” Int. J. Heat Mass Transf., **47**(14), pp. 3257–3268.

[8] Raghupathi, P. A., and Kandlikar, S. G., 2016, “Contact Line Region Heat Transfer Mechanisms for an Evaporating Interface,” Int. J. Heat Mass Transf., **95**, pp. 296–306.

[9] Wayner, P. C., 1979, “Effect of Thin Film Heat Transfer on Meniscus Profile and Capillary Pressure,” AIAA J., **17**(7), pp. 772–776.

[10] Holm, F. W., and Goplen, S. P., 1979, “Heat Transfer in the Meniscus Thin-Film Transition Region,” J. Heat Transf., **101**(3), pp. 543–547.

[11] Swanson, L. W., and Herdt, G. C., 1992, “Model of the Evaporating Meniscus in a Capillary Tube,” J. Heat Transf., **114**(2), pp. 434–441.

[12] Hallinan, K. P., Kim, S. J., and Chang, W. S., 1994, “Evaporation from an Extended Meniscus for Nonisothermal Interfacial Conditions,” J. Thermophys. Heat Transf., **8**(4), pp. 709–716.

[13] Khrustalev, D., and Faghri, A., 1996, “Fluid Flow Effects in Evaporation From Liquid–Vapor Meniscus,” J. Heat Transf., **118**(3), pp. 725–730.

[14] Kim, I. Y., and ayner, P. C., 1996, “Shape of an Evaporating Completely Wetting Extended Meniscus,” J. Thermophys. Heat Transf., **10**(2), pp. 320–325.

[15] Judd, R. L., and Hwang, K. S., 1976, “A Comprehensive Model for Nucleate Pool Boiling Heat Transfer Including Microlayer Evaporation,” ASME J Heat Transf., **98**(4), pp. 623–629.

[16] Sharp, R. R., 1964, *The Nature of Liquid Film Evaporation during Nucleate Boiling*, National Aeronautics and Space Administration.

[17] Voutsinos, C. M., and Judd, R. L., 1975, “Laser Interferometric Investigation of the Microlayer Evaporation Phenomenon,” J. Heat Transf., **97**(1), pp. 88–92.

[18] MacGregor, H. G., and Jawurek, H. H., 1992, “High Speed Ciné Laser Interferometry Technique for Microlayer Studies in Boiling,” NO J., **4**, pp. 1–7.

[19] Koffman, L. D., and Plesset, M. S., 1983, “Experimental Observations of the Microlayer in Vapor Bubble Growth on a Heated Solid,” J. Heat Transf., **105**(3), pp. 625–632.

[20] Gao, M., Zhang, L., Cheng, P., and Quan, X., 2013, “An Investigation of Microlayer beneath Nucleation Bubble by Laser Interferometric Method,” Int. J. Heat Mass Transf., **57**(1), pp. 183–189.

[21] Cooper, M. G., 1969, “The Microlayer and Bubble Growth in Nucleate Pool Boiling,” Int. J. Heat Mass Transf., **12**(8), pp. 915–933.

[22] van Ouwerkerk, H. J., 1971, “The Rapid Growth of a Vapour Bubble at a Liquid-Solid Interface,” Int. J. Heat Mass Transf., **14**(9), pp. 1415–1431.

[23] Graham, R. W., and Hendricks, R. C., 1967, “Assessment of Convection, Conduction, and Evaporation in Nucleate Boiling.”

[24] Dhavaleswarapu, H. K., Migliaccio, C. P., Garimella, S. V., and Murthy, J. Y., 2010, “Experimental Investigation of Evaporation from Low-Contact-Angle Sessile Droplets,” Langmuir, **26**(2), pp. 880–888.

[25] Chen, Z., Haginiwa, A., and Utaka, Y., 2017, “Detailed Structure of Microlayer in Nucleate Pool Boiling for Water Measured by Laser Interferometric Method,” Int. J. Heat Mass Transf., **108**, pp. 1285–1291.

[26] Utaka, Y., Kashiwabara, Y., and Ozaki, M., 2013, “Microlayer Structure in Nucleate Boiling of Water and Ethanol at Atmospheric Pressure,” Int. J. Heat Mass Transf., **57**(1), pp. 222–230.

[27] Young, T., 1805, “III. An Essay on the Cohesion of Fluids,” Philos. Trans. R. Soc. Lond., **95**, pp. 65–87.

[28] Shanahan, M. E. R., 1992, “Effects of Surface Flaws on the Wettability of Solids,” J. Adhes. Sci. Technol., **6**(4), pp. 489–501.

[29] Birdi, K. S., and Vu, D. T., 1993, “Wettability and the Evaporation Rates of Fluids from Solid Surfaces,” J. Adhes. Sci. Technol., **7**(6), pp. 485–493.

[30] Bourges-Monnier, C., and Shanahan, M. E. R., 1995, “Influence of Evaporation on Contact Angle,” Langmuir, **11**(7), pp. 2820–2829.

[31] Cazabat, A.-M., and Guéna, G., 2010, “Evaporation of Macroscopic Sessile Droplets,” Soft Matter, **6**(12), pp. 2591–2612.

[32] Orejon, D., Sefiane, K., and Shanahan, M. E. R., 2011, “Stick–Slip of Evaporating Droplets: Substrate Hydrophobicity and Nanoparticle Concentration,” Langmuir, **27**(21), pp. 12834–12843.

[33] Shanahan, M. E., 1995, “Simple Theory of" Stick-Slip" Wetting Hysteresis,” Langmuir, **11**(3), pp. 1041–1043.

[34] Deegan, R. D., Bakajin, O., Dupont, T. F., Huber, G., Nagel, S. R., and Witten, T. A., 2000, “Contact Line Deposits in an Evaporating Drop,” Phys. Rev. E, **62**(1), pp. 756–765.

[35] Moffat, J. R., Sefiane, K., and Shanahan, M. E. R., 2009, “Effect of TiO $_2$ Nanoparticles on Contact Line Stick−Slip Behavior of Volatile Drops,” J. Phys. Chem. B, **113**(26), pp. 8860–8866.

[36] Li, H., Fowler, N., Struck, C., and Sivasankar, S., 2011, “Flow Triggered by Instabilities at the Contact Line of a Drop Containing Nanoparticles,” Soft Matter, **7**(11), pp. 5116–5119.

[37] Anderson, D. M., and Davis, S. H., 1995, “The Spreading of Volatile Liquid Droplets on Heated Surfaces,” Phys. Fluids, **7**(2), pp. 248–265.

[38] Sefiane, K., and Tadrist, L., 2006, “Experimental Investigation of the De-Pinning Phenomenon on Rough Surfaces of Volatile Drops,” Int. Commun. Heat Mass Transf., **33**(4), pp. 482–490.

[39] Park, J., and Moon, J., 2006, “Control of Colloidal Particle Deposit Patterns within Picoliter Droplets Ejected by Ink-Jet Printing,” Langmuir, **22**(8), pp. 3506–3513.

[40] Calvert, P., 2001, “Inkjet Printing for Materials and Devices,” Chem. Mater., **13**(10), pp. 3299–3305.

[41] Yu, Y., Zhu, H., Frantz, J. M., Reding, M. E., Chan, K. C., and Ozkan, H. E., 2009, “Evaporation and Coverage Area of Pesticide Droplets on Hairy and Waxy Leaves,” Biosyst. Eng., **104**(3), pp. 324–334.

[42] Xia, D., and Brueck, S. R. J., 2008, “Strongly Anisotropic Wetting on One-Dimensional Nanopatterned Surfaces,” Nano Lett., **8**(9), pp. 2819–2824.

[43] Carroll, G. T., Wang, D., Turro, N. J., and Koberstein, J. T., 2006, “Photochemical Micropatterning of Carbohydrates on a Surface,” Langmuir, **22**(6), pp. 2899–2905.

[44] Kimura, M., Misner, M. J., Xu, T., Kim, S. H., and Russell, T. P., 2003, “Long-Range Ordering of Diblock Copolymers Induced by Droplet Pinning,” Langmuir, **19**(23), pp. 9910–9913.

[45] Nguyen, V. X., and Stebe, K. J., 2002, “Patterning of Small Particles by a Surfactant-Enhanced Marangoni-B\’enard Instability,” Phys. Rev. Lett., **88**(16), p. 164501.

[46] Jia, W., and Qiu, H., 2002, “Fringe Probing of an Evaporating Microdroplet on a Hot Surface,” Int. J. Heat Mass Transf., **45**(20), pp. 4141–4150.

[47] Schena, M., Shalon, D., Davis, R. W., and Brown, P. O., 1995, “Quantitative Monitoring of Gene Expression Patterns with a Complementary DNA Microarray,” Science, **270**(5235), pp. 467–470.

[48] Bensimon, D., Simon, A. J., Croquette, V., and Bensimon, A., 1995, “Stretching DNA with a Receding Meniscus: Experiments and Models,” Phys. Rev. Lett., **74**(23), pp. 4754–4757.

[49] Fang, X., Li, B., Petersen, E., Seo, Y.-S., Samuilov, V. A., Chen, Y., Sokolov, J. C., Shew, C.-Y., and Rafailovich, M. H., 2006, “Drying of DNA Droplets,” Langmuir, **22**(14), pp. 6308–6312.

[50] Dugas, V., Broutin, J., and Souteyrand, E., 2005, “Droplet Evaporation Study Applied to DNA Chip Manufacturing,” Langmuir, **21**(20), pp. 9130–9136.

[51] McHale, G., 2007, “Surface Free Energy and Microarray Deposition Technology,” Analyst, **132**(3), pp. 192–195.

[52] Kawase, T., Sirringhaus, H., Friend, R. H., and Shimoda, T., 2001, “Inkjet Printed Via-Hole Interconnections and Resistors for All-Polymer Transistor Circuits,” Adv. Mater., **13**(21), pp. 1601–1605.

[53] Jung, S., and Kim, H., 2015, “An Experimental Study on Heat Transfer Mechanisms in the Microlayer Using Integrated Total Reflection, Laser Interferometry and Infrared Thermometry Technique,” Heat Transf. Eng., **36**(12), pp. 1002–1012.

[54] Kim, H., and Buongiorno, J., 2011, “Detection of Liquid–Vapor–Solid Triple Contact Line in Two-Phase Heat Transfer Phenomena Using High-Speed Infrared Thermometry,” Int. J. Multiph. Flow, **37**(2), pp. 166–172.

[55] Raghupathi, P. A., and Kandlikar, S. G., 2017, “Pool Boiling Enhancement through Contact Line Augmentation,” Appl. Phys. Lett., **110**(20), p. 204101.

[56] Emery, T. S., Jaikumar, A., Raghupathi, P., Joshi, I., and Kandlikar, S. G., 2018, “Dual Enhancement in HTC and CHF for External Tubular Pool Boiling – A Mechanistic Perspective and Future Directions,” Int. J. Heat Mass Transf., **122**, pp. 1053–1073.